



The Large-scale Ionization Cones in the Galaxy

Joss Bland-Hawthorn^{1,2,3} , Philip R. Maloney⁴, Ralph Sutherland^{3,5} , Brent Groves⁵ , Magda Guglielmo¹, Wenhao Li¹,
Andrew Curzons¹, Gerald Cecil⁶, and Andrew J. Fox⁷ 

¹ Sydney Institute for Astronomy, School of Physics A28, University of Sydney, NSW 2006, Australia

² Miller Professor, Miller Institute, University of California, Berkeley, CA 94720, USA

³ ARC Centre of Excellence for All Sky Astrophysics in 3 Dimensions (ASTRO-3D), Australia

⁴ Private Astronomer, Boulder, CO 80301, USA

⁵ Research School of Astronomy & Astrophysics, Australia National University, Canberra 2611, Australia

⁶ Department of Physics and Astronomy, University of North Carolina, Chapel Hill, NC, USA

⁷ Space Telescope Science Institute, 3700 San Martin Drive, Baltimore, MD 21218, USA

Received 2018 July 9; revised 2019 August 24; accepted 2019 September 13; published 2019 November 18

Abstract

There is compelling evidence for a highly energetic Seyfert explosion (10^{56-57} erg) that occurred in the Galactic center a few million years ago. The clearest indications are the X-ray/ γ -ray “10 kpc bubbles” identified by the *ROSAT* and *Fermi* satellites. In an earlier paper, we suggested another manifestation of this nuclear activity, i.e., elevated $H\alpha$ emission along a section of the Magellanic Stream due to a burst (or flare) of ionizing radiation from Sgr A*. We now provide further evidence for a powerful flare event: UV absorption line ratios (in particular C IV/C II, Si IV/Si II) observed by the *Hubble Space Telescope* reveal that some Magellanic Stream clouds toward both galactic poles are highly ionized by a source capable of producing ionization energies up to at least 50 eV. We show how these are clouds caught in a beam of bipolar, radiative “ionization cones” from a Seyfert nucleus associated with Sgr A*. In our model, the biconic axis is tilted by about 15° from the south Galactic pole with an opening angle of roughly 60° . For the Magellanic Stream at such large Galactic distances ($D \gtrsim 75$ kpc), nuclear activity is a plausible explanation for all of the observed signatures: elevated $H\alpha$ emission and H ionization fraction ($x_e \gtrsim 0.5$), enhanced C IV/C II and Si IV/Si II ratios, and high C IV and Si IV column densities. Wind-driven “shock cones” are ruled out because the *Fermi* bubbles lose their momentum and energy to the Galactic corona long before reaching the Magellanic Stream. Our time-dependent Galactic ionization model (stellar populations, hot coronal gas, cloud–halo interaction) is too weak to explain the Magellanic Stream’s ionization. Instead, the nuclear flare event must have had a radiative UV luminosity close to the Eddington limit ($f_E \approx 0.1-1$). Our time-dependent Seyfert flare models adequately explain the observations and indicate that the Seyfert flare event took place $T_o = 3.5 \pm 1$ Myr ago. The timing estimates are consistent with the mechanical timescales needed to explain the X-ray/ γ -ray bubbles in leptonic jet/wind models ($\approx 2-8$ Myr).

Key words: galaxies: active – galaxies: Seyfert – Galaxy: evolution – Galaxy: nucleus – radiation mechanisms: non-thermal – shock waves

1. Introduction

One of the oldest baryonic remnants of the early universe in our Galaxy is the massive black hole in Sgr A*. At redshifts higher than $z \sim 4$, black holes are thought to grow rapidly through radiatively inefficient accretion (Inayoshi et al. 2016) and the merger of subsystems harboring lower-mass black holes (Volonteri 2010). After that time, the growth is regulated by the infall of gas, stars, and dark matter. The last few e -folds of mass over 10 Gyr are grown via radiatively *efficient* accretion (Rees & Volonteri 2007). The conversion efficiency must be $\epsilon \approx 10\%$ to explain the UV/X-ray background (Soltan 1982; Yu & Tremaine 2002; Zhang & Lu 2019). A black hole with mass M , today has converted $\epsilon M c^2$ of its rest mass into emergent energy. Over the past 10 Gyr, Sgr A*, for which $M = 4.15 \times 10^6 M_\odot$ (The GRAVITY Collaboration et al. 2019), must have released $\sim 10^{60}$ erg in relativistic particles and electromagnetic radiation to get to its current state.

In the Milky Way, we observe the X-ray/ γ -ray bubbles with an inferred energy of $10^{56}-10^{57}$ erg. The first evidence of a kiloparsec-scale outflow in the Galaxy came from bipolar *ROSAT* 1.5 keV X-ray emission inferred to be associated with the Galactic center (Bland-Hawthorn & Cohen 2003). In Figure 1, this same component is directly associated with the

Fermi γ -ray bubbles (1–100 GeV) discovered by Su et al. (2010). Star formation activity fails on energetic grounds by a factor of 400 based on what we see today (Miller & Bregman 2016), or ~ 100 if we allow for past starbursts within the limits imposed by the resolved stellar population (Bland-Hawthorn et al. 2013, hereafter BH2013; Nataf 2016).

The source of the X-ray/ γ -ray bubbles can only be from nuclear activity: all contemporary leptonic models of the X-ray/ γ -ray bubbles agree on this point, with timescales for the event falling in the range of 2–8 Myr (Guo & Mathews 2012; Miller & Bregman 2016; Narayanan & Slatyer 2017; see Carretti et al. 2013). These must be driven by the active galactic nucleus (AGN; jet and/or accretion disk wind) on a timescale of order a few megayears—for a comprehensive review, see Yang et al. (2018).

AGN jets are remarkably effective at blowing bubbles regardless of the jet orientation because the jet head is diffused or deflected by each interaction with density anomalies in a fractal interstellar medium (ISM; Zovaro et al. 2019). The evidence for an active jet today in the Galactic center is weak (Bower & Backer 1998). Su & Finkbeiner (2012) found a jet-like feature in γ -rays extending from $(\ell, b) \approx (-11^\circ, 44^\circ)$ to $(11^\circ, -44^\circ)$; this axis is indicated in Figure 2. In recent simulations, the AGN jet drills its way through the multiphase

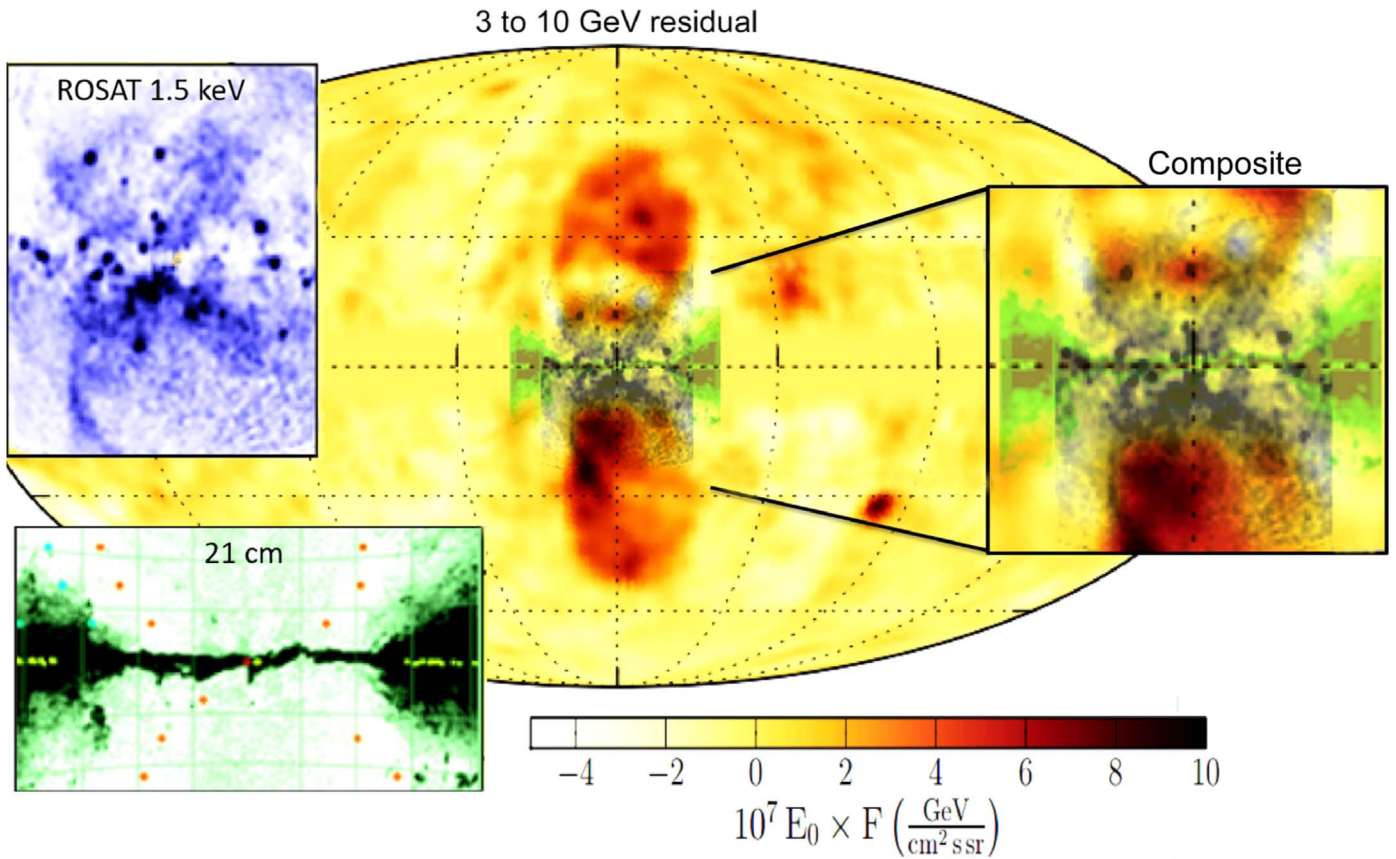


Figure 1. All-sky Mollweide projection (NGP uppermost) aligned with the Galactic center showing the strong association between the 3–10 GeV γ -ray emission (Ackermann et al. 2014; main image), the 1.5 keV X-ray emission (Bland-Hawthorn & Cohen 2003; blue inset), and the 21 cm cold hydrogen emission (Lockman & McClure-Griffiths 2016; green inset with orange dots spaced 1 kpc apart at the distance of the Galactic center). On the right-hand side, we show a magnified region around the Galactic center as a color composite with all three components overlaid.

ISM with a speed of roughly 1 kpc Myr^{-1} (Mukherjee et al. 2018, Appendix A). If the tentative claims are not confirmed, this may indicate that either the AGN outflow was not accompanied by a jet or the jet has already pushed through the inner disk gas and has now dispersed.

Absorption-line UV spectroscopy of background AGNs and halo stars reveals cool gas clouds entrained in the outflow (Fox et al. 2015; Bordoloi et al. 2017; Savage et al. 2017; Karim et al. 2018); HI clouds are also seen (Di Teodoro et al. 2018). Modeling of the cloud kinematics yields similar timescales for the wind ($\sim 6\text{--}9 \text{ Myr}$; Fox et al. 2015; Bordoloi et al. 2017). An updated shock model of the O VII and O VIII X-ray emission over the bubble surfaces indicates that the initial burst took place $4 \pm 1 \text{ Myr}$ ago (Miller & Bregman 2016).

A number of authors (e.g., Zubovas & Nayakshin 2012) tie the *localized* X-ray/ γ -ray activity to the formation of the young stellar annulus ($M_* \sim 10^4 M_\odot$) in orbit about the Galactic center (see Koyama 2018). These stars, with uncertain ages in the range of 3–8 Myr, are mostly on elliptic orbits and stand out in a region dominated by an old stellar population (Paumard et al. 2006; Yelda et al. 2014). A useful narrative of how this situation can arise is given by Lucas et al. (2013): a clumpy prolate cloud with a dimension of order the impact radius, and oriented perpendicular to the accretion plane, sets up accretion timescales that can give rise to high-mass stars in elliptic prograde and retrograde orbits.

Nuclear activity peaked during the golden age of galaxy formation ($z = 1\text{--}3$; Hopkins & Beacom 2006), but it is

observed to occur in a few percent of galaxies at lower levels today. Given that most galaxies possess nuclear black holes, this activity may be ongoing and stochastic in a significant fraction, even if only detectable for a small percentage of sources at a given epoch (Novak et al. 2011). If most of the activity occurred after $z \sim 1$, this argues for *Fermi* bubble-like outbursts roughly every $\sim 10 \text{ Myr}$ or so. Each burst may have lasted up to $\sim 1 \text{ Myr}$ at a time (Guo & Mathews 2012), flickering on shorter timescales. This implies that $\sim 10\%$ of all galaxies are undergoing a Seyfert phase at any time but where most outcomes, like the *Fermi* bubbles, are not easily detectable (see Sebastian et al. 2019).

Independent of the mechanical timescales, BH2013 show that the high levels of $H\alpha$ emission along the Magellanic Stream are consistent with a Seyfert ionizing flare event 2–3 Myr ago (see Figure 2); starburst-driven radiation fails by two orders of magnitude. Ionization cones are not uncommon in active galaxies today (e.g., Pogge 1988; Tsvetanov et al. 1996) and can extend to $\sim 100 \text{ kpc}$ distances (Kreimeyer & Veilleux 2013). Here we revisit our earlier work in light of new observations and a better understanding of the Magellanic Stream’s distance from the Galaxy. In Section 2, we update what has been learned about the ionization, metallicity, and gas content of the Magellanic Stream and its orbit properties. Section 3 builds up a complete model of the Galactic UV radiation field and includes a major AGN contribution to illustrate the impact of nuclear activity. In Section 4, we carry out time-dependent ionization calculations to update the likely

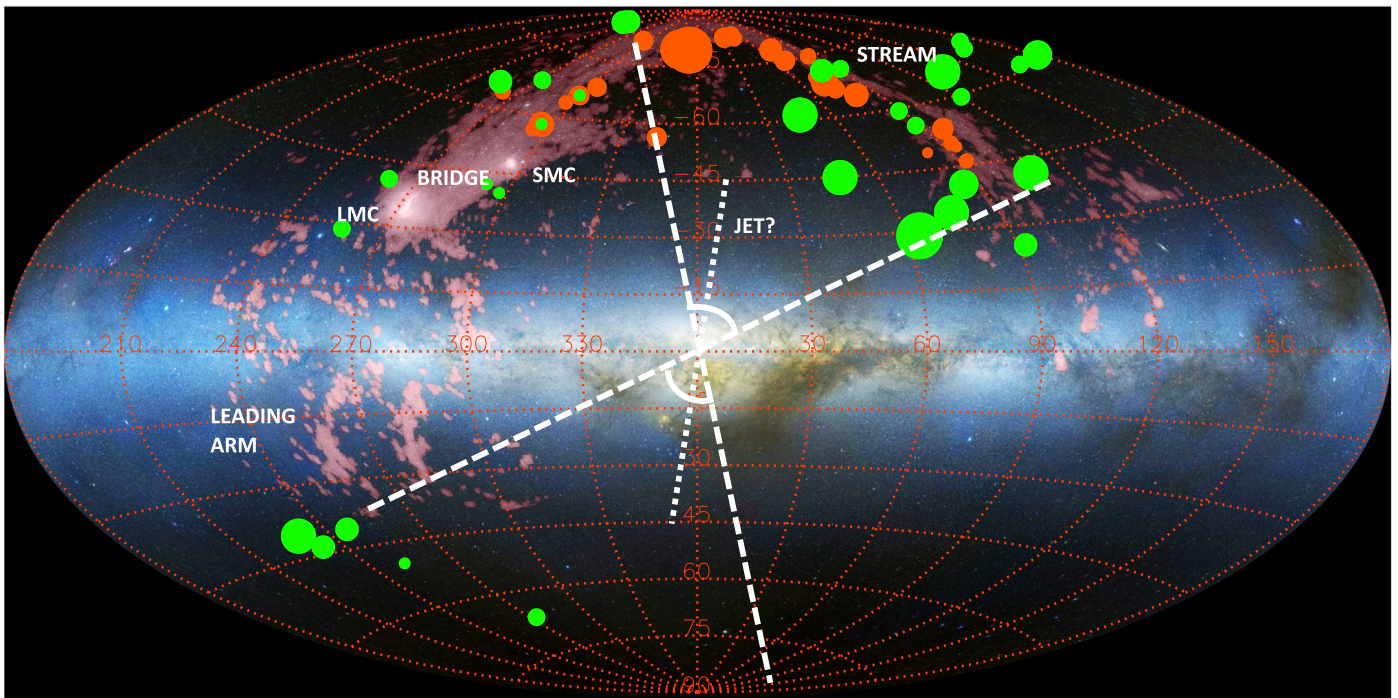


Figure 2. Rotated all-sky Aitoff projection (south Galactic pole uppermost) aligned with the Galactic center showing the orientation of the ionization cones (Section 4) inferred from this work. The 3D space orientation is uncertain: the opening angle is roughly 60° and includes the Galactic polar axis. The red points indicate the $H\alpha$ detections, where the symbol size scales with the surface brightness; the green points scale with the strength of the C IV/C II ratio, with larger points indicating a harder radiation field (if photoionized). The optical image and 21 cm overlay (pink) were first presented by Nidever et al. (2008); the radio emission is from the 21 cm H I mapping of the Magellanic Clouds and Stream (including the leading arms) by Kalberla et al. (2005). Note that some Magellanic Stream H I clouds fall within the cones (indicated by small arcs) in both hemispheres. The dotted line indicates the axis of a putative radio/ γ -ray jet (Bower & Backer 1998; Su & Finkbeiner 2012).

timescale for the Seyfert flare. Section 5 concludes with suggested follow-up observations and discusses the implications of our findings.

2. New Observations

2.1. Magellanic Stream: Gas and Metal Content

Since its discovery in the 1970s, many authors have studied the physical properties of the gas along the Magellanic Stream (Putman et al. 1998; Brüns et al. 2005; Kalberla et al. 2005; Stanimirović et al. 2008; Fox et al. 2010; Nigra et al. 2012). The Magellanic Stream lies along a great arc that spans more than half the sky (e.g., Nidever et al. 2010). Its metallicity content is generally about 1/10 of the solar value, consistent with the idea that the gas came from the SMC and/or the outer regions of the LMC (Fox et al. 2013), although a filament tracing back to the inner LMC has an elevated level of metal enrichment (Richter et al. 2013). The inferred total mass of the Magellanic Stream is ultimately linked to its distance D from the Galactic center. The total H I mass of the Magellanic gas system (corrected for He) is $5 \times 10^8 (D/55 \text{ kpc})^2 M_\odot$ (Brüns et al. 2005), but this may not even be the dominant mass component (Bland-Hawthorn et al. 2007; d’Onghia & Fox 2016). Fox et al. (2014) find that the plasma content may dominate over the neutral gas by a factor of a few such that the Magellanic Stream’s total gas mass is closer to $2.0 \times 10^9 (D/55 \text{ kpc})^2 M_\odot$. We discuss the likely value of D measured along the south Galactic pole (SGP) in the next section.

2.2. Magellanic Stream: Orbit Trajectory

The precise origin of the trailing and leading arms of the Magellanic Stream is unclear. Theoretical models for the Magellanic Stream date back to at least the early seminal work of Fujimoto & Sofue (1976, 1977). For three decades, in the absence of a distance indicator, the Magellanic Stream’s distance over the SGP was traditionally taken to be the midpoint in the LMC and SMC distances, i.e., $D = 55 \text{ kpc}$, a distance that is now thought to be too small.

In a series of papers, Kallivayalil and collaborators show that the proper motions of the LMC and SMC are 30% higher than original long-standing estimates (e.g., Kallivayalil et al. 2006, 2013). Over the same period, mass estimates of the Galaxy have decreased to $M_{\text{vir}} = (1.3 \pm 0.3) \times 10^{12} M_\odot$ (see Bland-Hawthorn & Gerhard 2016; McMillan 2017). Thus, the orbit of the Magellanic System must be highly elliptic. Contemporary models consider the LMC and SMC to be on their first infall with an orbital period of order a Hubble time (Besla et al. 2007, 2012; Nichols et al. 2011).

The Magellanic Stream is a consequence of the tidal interaction between both dwarfs. The models move most of the trailing Magellanic Stream material to beyond 75 kpc over the SGP. Here we take a representative model for the Magellanic Stream particles from a recent hydrodynamical simulation (Guglielmo et al. 2014), adopting a smooth fit to the centroid of the particle trajectory and some uncertainty about that trajectory.

In passing, we note that while the trailing Magellanic Stream is understood in these models, the “leading arm” is unlikely to be explained as a tidal extension in the same way because of

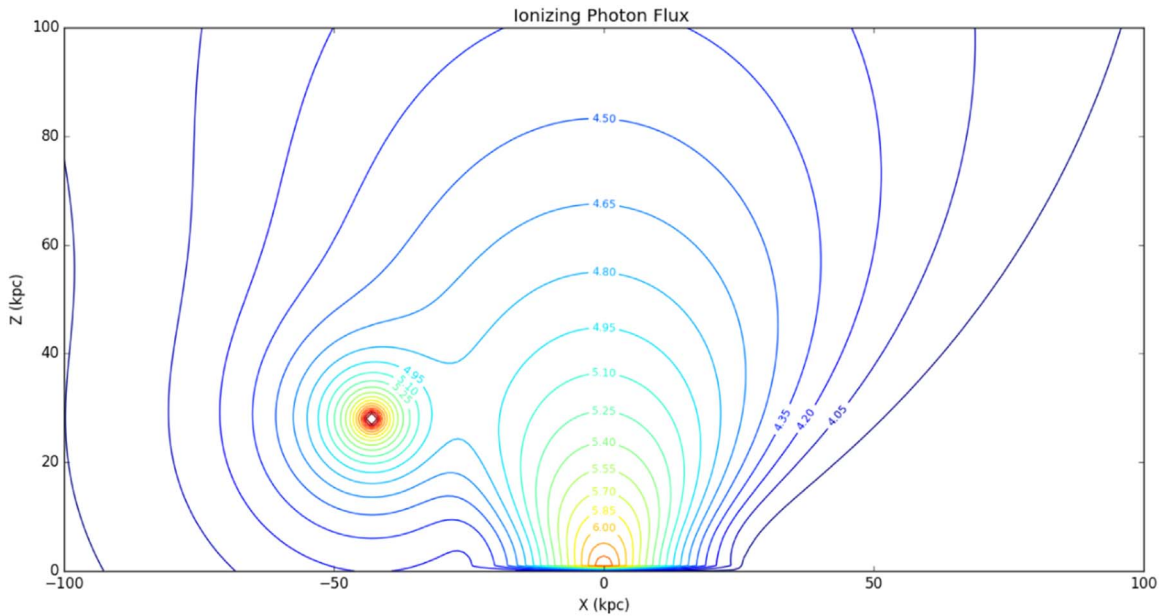


Figure 3. Our model for the ionizing radiation field over the south Galactic hemisphere arising from the opaque Galactic disk and the LMC (Section 3). The units of the contours are $\log(\text{photons cm}^{-2} \text{s}^{-1})$. Small contributions from the hot Galactic corona and the cosmic UV background are also included. The X - Z plane runs through the LMC, the SGP, and the Galactic center defined by the plane of Magellanic longitude. The ionizing flux contours are spaced in equal log intervals.

the strong ram pressure confinement imposed by the Galactic corona ahead of the Magellanic Clouds (Tepper-Garcia et al. 2019). Instead, it may be debris arising from an earlier interaction of the LMC-SMC system protected by a Magellanic corona, for example. Thus, the origin of the “leading arm” is unclear, and its distance is poorly constrained. Most of the cool gas ahead of the Magellanic Clouds lies outside of the ionization cones in Figure 2.

2.3. Magellanic Stream: Ionization

Weiner & Williams (1996) first discovered elevated levels of $H\alpha$ emission along the Magellanic Stream, detections that have been confirmed and extended through follow-up observations (Weiner et al. 2002; Putman et al. 2003; BH2013; Barger et al. 2017). There have been several attempts to understand this emission over the past two decades in terms of Galactic sources (Bland-Hawthorn & Maloney 1999), particle trapping by magnetic fields (Konz et al. 2001), thermal conduction and mixing (Fox et al. 2005), cloud-halo interactions (Weiner & Williams 1996), and cloud-cloud interactions (Bland-Hawthorn et al. 2007).

While these sources can contribute to ionization and heating along the Magellanic Stream, in light of new evidence, we believe that only the Seyfert flare model (BH2013) survives as a likely candidate for the brightest emission. Further evidence for nonthermal photons being the source of the ionization comes from a UV spectroscopic study carried out with the *Hubble Space Telescope* (*HST*) of distant quasars that lie behind the Magellanic Stream. Fox et al. (2014) infer ionization levels along the Magellanic Stream from UV absorption features arising from H I, Si II, Si III, Si IV, C II, and C IV. They find that there are three patches along the Magellanic Stream that require enhanced levels of hard ionization (30–50 eV photons) relative to stellar photons. One is highly localized at the LMC; the other regions lie toward the north Galactic pole (NGP) and SGP. We argue below that these

regions fall within the “ionization cones” of the Seyfert event. These data are presented and modeled in Section 4.

3. New Models

3.1. Galactic Ionization Model

We model the Magellanic Stream $H\alpha$ emission and carbon absorption features using the Galactic ionization model presented by Bland-Hawthorn & Maloney (1999, 2002), updated with the time-dependent calculations in BH2013. A cross section through the 3D model across the south Galactic hemisphere passing through the Galactic center and the LMC is shown in Figure 3. The Galactic disk parameters remain unchanged from earlier work where we considered the expected emission arising from stars. The total flux at a frequency ν reaching an observer located at a distance D is obtained from integrating the specific intensity I_ν over the surface of a disk, i.e.,

$$F_\nu = \int_A I_\nu(\mathbf{n})(\mathbf{n}\cdot\mathbf{N}) \frac{dA}{D^2}, \quad (1)$$

where \mathbf{n} and \mathbf{N} are the directions of the line of sight and the outward normal to the surface of the disk, respectively. In order to convert readily to an $H\alpha$ surface brightness, we transform Equation (1) to a photon flux after including the effect of disk opacity τ_D at the Lyman limit such that

$$\varphi_\star = \int_\nu \frac{F_\nu}{h\nu} \exp(-\tau_D / \cos\theta) \cos\theta \, d\nu, \quad (2)$$

for which $|\theta| \neq \pi/2$ and where φ_\star is the photoionizing flux from the stellar population, $\mathbf{n}\cdot\mathbf{N} = \cos\theta$, and h is Planck’s constant. This is integrated over frequency above the Lyman limit ($\nu = 13.6 \text{ eV}/h$) to infinity to convert to units of photon flux ($\text{photons cm}^{-2} \text{s}^{-1}$). The mean vertical opacity of the disk over the stellar spectrum is $\tau_D = 2.8 \pm 0.4$, equivalent to a

vertical escape fraction of $f_{*,\text{esc}} \approx 6\%$ perpendicular to the disk ($n \cdot N = 1$).

The photon spectrum of the Galaxy is a complex time-averaged function of energy N_* (photon rate per unit energy) such that $4\pi D^2 \varphi_* = \int_0^\infty N_*(E) dE$. For a given ionizing luminosity, we can determine the expected $\text{H}\alpha$ surface brightness at the distance of the Magellanic Stream. For an optically thick cloud ionized on one side, we relate the emission measure to the ionizing photon flux using $\mathcal{E}_m = 1.25 \times 10^{-6} \varphi_* \text{ cm}^{-6} \text{ pc}$ (Bland-Hawthorn & Maloney 1999). In Appendix A, we relate \mathcal{E}_m to the more familiar millirayleigh units (mR) used widely in diffuse detection work.

The Galactic UV contribution at the distance D of the Magellanic Stream is given by

$$\mu_{*,\text{H}\alpha} = 10 \zeta \left(\frac{f_{*,\text{esc}}}{0.06} \right) \left(\frac{D}{75 \text{ kpc}} \right)^{-2} \text{ mR}. \quad (3)$$

The correction factor $\zeta \approx 2$ is included to accommodate weakly constrained ionizing contributions from old stellar populations and fading supernova bubbles in the disk (BH2013).

After Barger et al. (2013) and Fox et al. (2014), we incorporate the UV contribution from the LMC but with an important modification. Barger et al. (2013) showed how the LMC UV ionizing intensity is sufficient to ionize the Magellanic Bridge in close proximity; the SMC UV radiation field can be neglected. This is assisted by the orientation of the LMC disk with respect to the Magellanic Bridge. In our treatment, the LMC’s greater distance and orientation do not assist the ionization of the Magellanic Stream. We treat the LMC as a point source with a total ionizing luminosity reduced by a factor $\exp(-\tau_L)$; $\tau_L = 1.7$ is the mean LMC disk opacity that we scale from the Galactic disk opacity ($\tau_D = 2.8$) by the ratio of their metallicities (Fox et al. 2014).

We stress that the LMC cannot be the source of the Magellanic Stream ionization. Its imprint over the local HI is clearly seen in Barger et al. (2013, Figure 16). One interesting prospect, suggested by the referee, is that one or more ultraluminous X-ray sources (ULXs) in the LMC have produced a flash of hard UV/X-ray radiation in the recent past. In fact, a few such sources are observed there (Kaaret et al. 2017) and may be responsible for the localized C IV/C II enhancement at the LMC (Fox et al. 2014). We include the super-Eddington accretion spectrum in our later models (Sections 4.3, 4.4.1) to emphasize this point.

Other sources—We have used updated parameters for the Galactic corona from Miller & Bregman (2016), but the UV emission from the halo remains negligible (i.e., a few percent at most) compared to the Galactic disk ($\varphi_* \sim 5 \times 10^4 \text{ photons cm}^{-2} \text{ s}^{-1}$ at 75 kpc along the SGP). The cosmic ionizing intensity is taken from Weymann et al. (2001), but this is of the same order as the hot corona ($\varphi_* \lesssim 10^{3.5} \text{ photons cm}^{-2} \text{ s}^{-1}$ at 75 kpc). An earlier model attempted to explain the emission in terms of the Magellanic Stream’s interaction with the halo (Bland-Hawthorn et al. 2007). The direct interaction of the clouds with the coronal gas is too weak to generate sufficient emission through collisional processes, but these authors show that a “shock cascade” arises if sufficient gas is stripped from the clouds such that the following clouds collide with the ablated material. This can be made to work if the Magellanic Stream is moving through

comparatively dense coronal material ($n_{\text{hot}} \sim 10^{-4} \text{ cm}^{-3}$). But the greater Magellanic Stream distance ($D \gtrsim 75 \text{ kpc}$; e.g., Jin & Lynden-Bell 2008) makes this less likely (Tepper-Garcia et al. 2015). Barger et al. (2017) adopt a massive hot halo in order to maximize the contribution from the shock cascade; whether such a corona is possible is still an open question (see Faerman et al. 2017; Bregman et al. 2018).

The shock cascade model as presented above struggles to produce a Magellanic Stream $\text{H}\alpha$ background of $\sim 100 \text{ mR}$, although there are other factors to consider in future models. The respective roles of magnetic fields (Konz et al. 2001), thermal conduction (Vieser & Hensler 2007), and turbulent mixing (Li et al. 2019) have not been considered together in a dynamic turbulent boundary layer. They can work for or against each other in amplifying the observed recombination emission. Radiative/particle MHD models on galactic scales are in their infancy (Sutherland 2010; Bland-Hawthorn et al. 2015) but will need to be addressed in future years.

3.2. Seyfert Ionization Model

If the Galaxy went through a Seyfert phase in the recent past, it could conceivably have been so UV-bright that it lit up the Magellanic Stream over the SGP through photoionization (Figure 4). The Magellanic Stream has detectable $\text{H}\alpha$ emission along its length five times more luminous than can be explained by UV escaping from the Galactic stellar population or an earlier starburst (BH2013, Appendix B). The required star formation rate is at least two orders of magnitude larger than allowed by the recent star formation history of the Galactic center (see Section 2). An accretion flare from Sgr A* is a much more probable candidate for the ionization source because (a) an accretion disk converts gas to ionizing radiation with much greater efficiency than star formation, thus minimizing the fueling requirements; and (b) there is an abundance of material in the vicinity of Sgr A* to fuel such an outburst.

We now consider the impact of past Seyfert activity using arguments that are independent of the X-ray/ γ -ray mechanical timescales (Section 1) but consistent with them. We derive the likely radiation field of an accretion disk around a supermassive black hole. BH2013 show how a Seyfert flare with an AGN spectrum that is 10% of the Eddington luminosity ($f_E = 0.1$) for a $4 \times 10^6 M_\odot$ black hole can produce sufficient UV radiation to ionize the Magellanic Stream ($D \gtrsim 50 \text{ kpc}$). But since Sgr A* is quiescent today, what we see has faded significantly from the original flash. $\text{H}\alpha$ recombines faster than the gas cools for realistic gas densities ($n_e \sim 0.1\text{--}1 \text{ cm}^{-3}$) and the well-established Magellanic Stream metallicity ($Z \approx 0.1 Z_\odot$; Fox et al. 2013). Thus, they find that the event must have happened within the past few million years, consistent with jet-driven models of the 10 kpc bipolar bubbles. This timescale includes the double-crossing time (the time for the flare radiation to hit the Magellanic Stream + the time for the recombination flux to arrive at Earth), the time for the ionization front to move into the neutral gas, and the recombination time.

Accretion disk model—The Shakura–Sunyaev treatment for subcritical accretion produces a thin Keplerian disk that can cool on an infall timescale, leading to a wide-angle thermal broadband emitter. They assumed that an unknown source of turbulent stress generated the viscosity, e.g., through strong shearing in the disk. But magnetorotational instability has supplanted hydrodynamical turbulence because even a weak magnetic field threaded through the disk suffices to trigger the

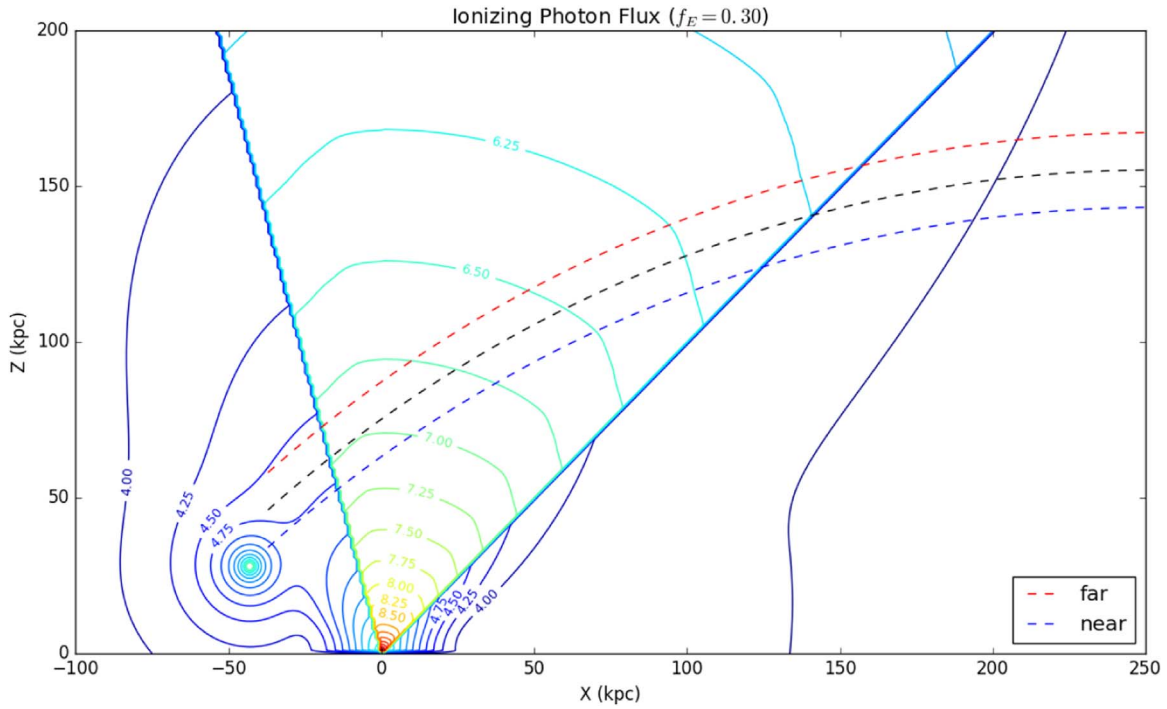


Figure 4. Ionizing field presented in Figure 3 with the added contribution of a Seyfert flare event, but shown on a larger physical scale. The units of the contours are $\log(\text{photons cm}^{-2} \text{s}^{-1})$. For illustration, we show the impact of a sub-Eddington flare ($f_E = 0.3$). This flux level is needed to reproduce what we observe but is inconsistent with Sgr A* activity today. A more likely scenario is that the event occurred in the past and what is seen today is the fading recombination of this flare (BH2013). The black trajectory is a fit to the orbit path of the Magellanic Stream particles (Guglielmo et al. 2014), which uses updated parameters for the Galaxy and is quite typical of modern simulations. The blue and red tracks represent the 3σ uncertainties for the distribution of Magellanic Stream particles. The ionizing flux contours are spaced in equal log intervals. A schematic movie of a pulsing AGN radiation field is available at http://www.physics.usyd.edu.au/~jhb/share/Movies/SgrA_ionized_cone.gif. We also include a simulation of a flickering AGN radiation field (Novak et al. 2011) impinging on the Magellanic Stream at http://www.physics.usyd.edu.au/~jhb/share/Movies/MilkyWay_ionized_cone.mp4; the movie ends when the Magellanic Clouds reach their observed position today.

onset of viscosity (Balbus & Hawley 1991). The maximum temperature of the thin disk is

$$T_{\max}(r) \approx 54 (r/r_s)^{-3/4} M_{*,8}^{-1/4} f_E^{1/4} \text{ eV}, \quad (4)$$

where $M_{*,8}$ is the mass of the black hole in units of $10^8 M_\odot$ (Novikov & Thorne 1973). Thus, the continuum radiation peaks above 100 eV for a subcritical accretion disk orbiting the black hole in Sgr A*, which is sufficiently hardened to account for the anomalous Magellanic Stream ionization observed in UV absorption lines (Fox et al. 2014). Strictly speaking, T_{\max} is for a maximally rotating (Kerr) black hole; we need to halve this value for a stationary black hole.

In order to account for the mechanical luminosity of the X-ray/ γ -ray bubbles, various authors (e.g., Zubovas & King 2012; Nakashima et al. 2013) argue for an even more powerful outburst of order the Eddington luminosity ($f_E \approx 1$). A quasi- or super-Eddington event in fact helps all aspects of our work. This is more likely to generate sufficient UV to explain the Magellanic Stream’s ionization while providing sufficient mechanical luminosity to drive a powerful jet or wind. But the Shakura–Sunyaev algebraic formalism breaks down at high mass accretion rates ($f_E > 0.3$), forming a geometrically thick, radiation-supported torus. These develop a central funnel around the rotation axis from which most of the radiation arises. In Figure 4, the radiation field and spectral hardness now have a strong dependence on polar angle (e.g., Paczynski & Wiita 1980; Madau 1988). The hot funnels may

help to accelerate material along collimated jets (Abramowicz & Piran 1980), which could further harden the radiation field and constrict the ionization pattern.

In Figure 5, we adopt the thick accretion disk model of Madau (1988), which ventures into the domain of mildly super-Eddington accretion rates. (A supplementary discussion of this model is provided by Acosta-Pulido et al. 1990.) The specific intensity of the thick disk (in units of $\text{erg cm}^{-2} \text{s}^{-1} \text{Hz}^{-1}$) is given by

$$4\pi I_\nu = 1.0 \times 10^{-14} T_s^{11/4} [\beta/(1-\beta)]^{1/2} \times x^{3/2} e^{-1} (1 - e^{-x})^{-1/2}, \quad (5)$$

where $x = h\nu/kT_s$, β is the ratio of the gas pressure to the total pressure ($\sim 10^{-4}$), and T_s is the disk surface temperature, which has a weak dependence on the black hole mass and other factors, i.e., $T_s \propto M_{*,8}^{-4/15} \beta^{-2/15}$. This parametric model allows us to compute the ionizing spectrum for different viewing orientations of the disk.

The most important attribute of an accretion disk model for our work is the photon flux and primary geometric parameters (e.g., inner and outer cutoff radii), with other considerations like spectral shape being of secondary importance (Tarter et al. 1969; Dove & Shull 1994; Maloney 1999). Madau (1988) includes a correction for scattering off the inner funnel that tends to harden the ionizing spectrum and boost its intensity. But it does not necessarily generate highly super-Eddington luminosities owing to advection of heat onto the black hole (Madau et al. 2014, Figure 1). In Section 4.3, we consider a

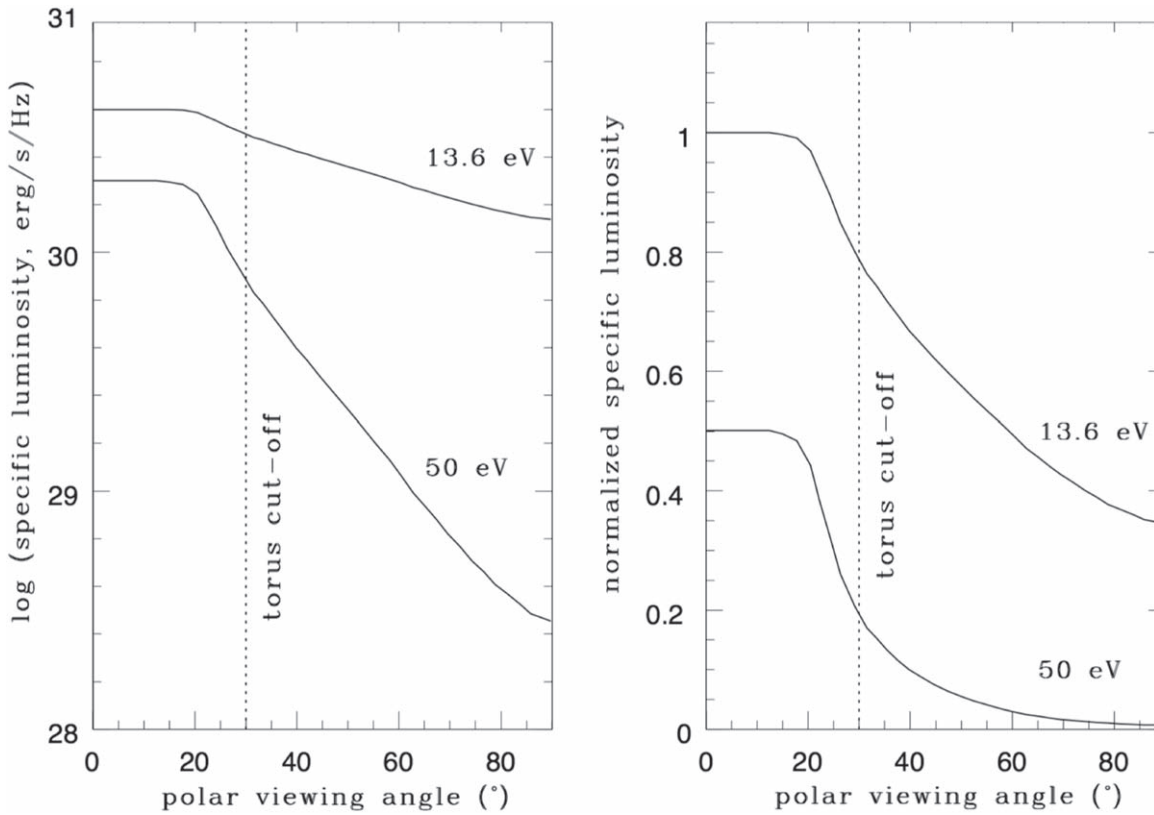


Figure 5. Accretion disk model (Madau 1988; Madau et al. 2014) for high mass accretion rates. The thick disk is defined within $r \lesssim 500 r_g \approx 20$ au, where $r_g = GM/c^2$ is the black hole gravitational radius. It produces an ionizing radiation field that is strongly dependent on viewing angle and photon energy. The vertical dashed line indicates the cutoff imposed by the dusty torus on much larger physical scales. Left: specific luminosity as a function of angle from the SGP evaluated at two different photon energies. Right: same model as in the left panel, but now plotted on a linear scale, normalized at the Lyman limit, to emphasize the self-truncation of the disk radiation field, particularly at higher energies.

broad range of ionizing continua to uncover how the spectral hardness in the 10–100 eV window influences the predicted UV diagnostics.

4. UV Ionization of the Magellanic Stream

4.1. Expected Emission from an Active Nucleus

An accreting black hole converts rest-mass energy with an efficiency factor ϵ ($\sim 10\%$) into radiation with a luminosity $L_* = \epsilon \dot{m} c^2 = 2\epsilon \dot{M} M_* / r_s$, for which \dot{m} is the mass accretion rate and r_s is the Schwarzschild radius; for a recent review, see Zhang & Lu (2019). The accretion disk luminosity can limit the accretion rate through radiation pressure; the Eddington limit is given by $L_E = 4\pi GM_* m_p c \sigma_T^{-1}$, where σ_T is the Thomson cross section for electron scattering. For the condition $L_* = L_E$, radiation pressure from the accretion disk at the Galactic center limits the maximum accretion rate to $\dot{m} \sim 0.2 M_\odot \text{ yr}^{-1}$. AGNs appear to spend most of their lives operating at a fraction f_E of the Eddington limit, with rare bursts arising from accretion events (Hopkins & Hernquist 2006). The orbital period of the Magellanic System is of order a Hubble time (Besla et al. 2012), so we can consider the Magellanic Stream to be a stationary target relative to ionization timescales.

BH2013 show that for an absorbing cloud that is optically thick, the ionizing flux can be related directly to an H α surface

brightness. The former is given by

$$\varphi_* = 1.1 \times 10^6 \left(\frac{f_E}{0.1} \right) \left(\frac{f_{*,\text{esc}}}{1.0} \right) \left(\frac{D}{75 \text{ kpc}} \right)^{-2} \text{ phot cm}^{-2} \text{ s}^{-1}. \quad (6)$$

The dust levels are very low in the Magellanic Stream, consistent with its low metallicity (Fox et al. 2013). We have included a term for the UV escape fraction from the AGN accretion disk $f_{*,\text{esc}}$ ($n.N = 1$). The spectacular evacuated cavities observed at 21 cm by Lockman & McClure-Griffiths (2016) suggest that there is little to impede the radiation along the poles, at least on large scales (Figure 1). Some energy is lost owing to Thomson scattering, but this is only a few percent in the best-constrained sources (e.g., NGC 1068; Krolik & Begelman 1986). In principle, the high value of $f_{*,\text{esc}}$ can increase $f_{*,\text{esc}}$, but the stellar bulge is not expected to make more than a 10%–20% contribution to the total stellar budget (Bland-Hawthorn & Maloney 2002); a possible contribution is accommodated by the factor ζ (Equation (3)).

The expected surface brightness for clouds that lie within an “ionization cone” emanating from the Galactic center is given by

$$\mu_{*,\text{H}\alpha} = 440 \left(\frac{f_E}{0.1} \right) \left(\frac{f_{*,\text{esc}}}{1.0} \right) \left(\frac{D}{75 \text{ kpc}} \right)^{-2} \text{ mR}. \quad (7)$$

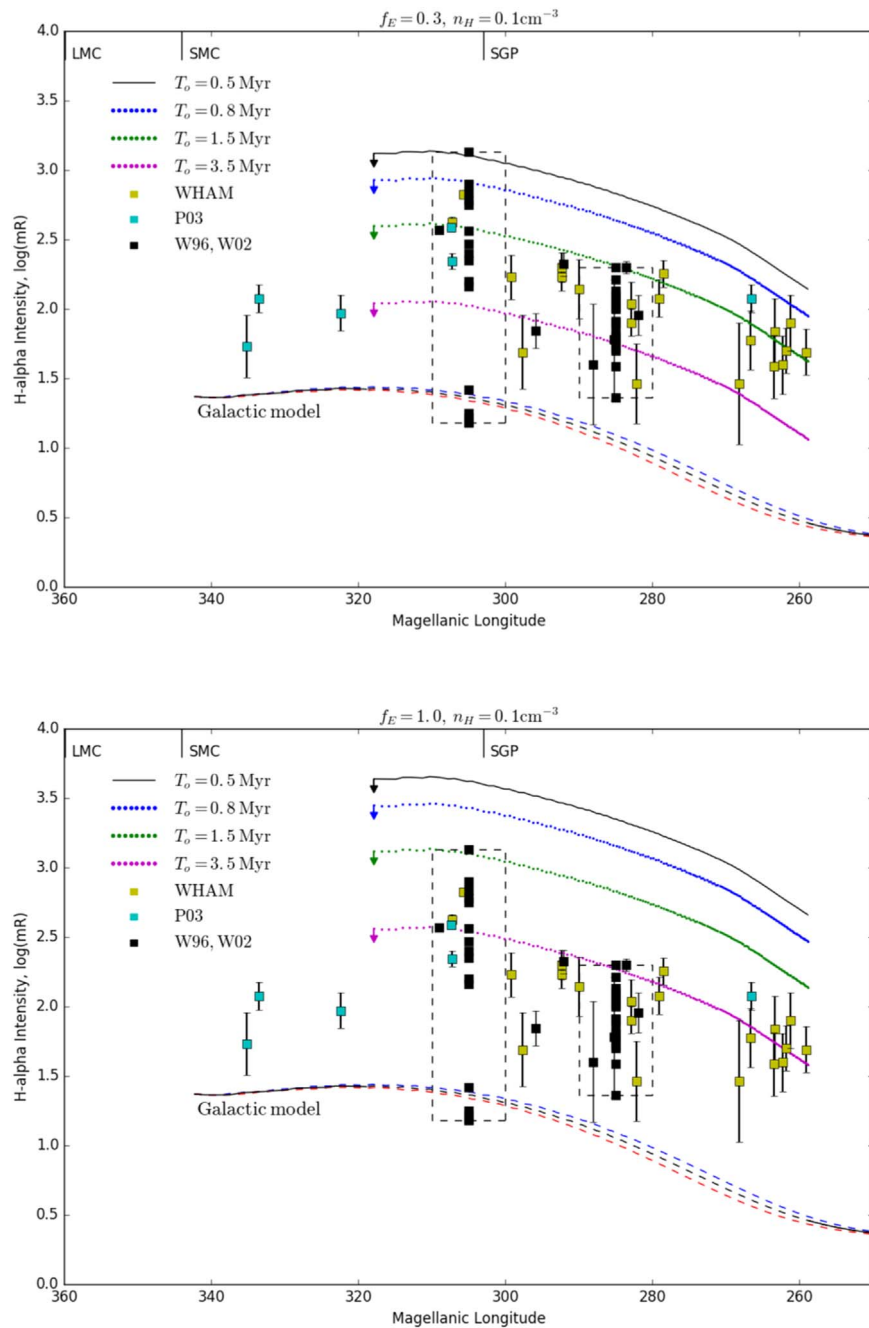


Figure 6. Predicted $H\alpha$ intensity along the Magellanic Stream ($D = 75$ kpc) as a function of Magellanic longitude. The data points are taken from Weiner & Williams (1996, W96), Weiner et al. (2002, W02), the WHAM Survey (BH2013), and Putman et al. (2003, P03). W96 and W02 are small-aperture measurements within a 10° window at unpublished sky positions. The longitudes of the LMC, SMC, and SGP are indicated. The topmost continuous black track corresponds to the middle track shown in Figure 4 for $f_E = 0.3$; this is the instantaneous $H\alpha$ emission in the flash at $T_o = 0$ for optically thick gas. But since Sgr A* is in a dormant state, what we see today must have faded from the initial flash. We show the predicted trend for the $H\alpha$ emission after 0.8 and 1.5 Myr (which includes 0.5 Myr for the light-crossing time to the Magellanic Stream and back) for an assumed density of $n_H = 0.1 \text{ cm}^{-3}$. The density cannot be much lower if we are to produce the desired $H\alpha$ emission; a higher density reduces the fading time. The downward-pointing arrows indicate where the in-cone predicted emission drops to the Galactic model outside of the cones. This is shown as dashed lines along the bottom.

This provides us with an upper limit or “peak brightness” along the spin axis of the accretion disk assuming that our model is correct. A few of the clumps exceed $\mu(H\alpha) \approx 440$ mR in Figure 6 by about a factor of 2. Our model parameters are only approximate.

Equation (7) is also applicable to isotropic emission within the ionization cone from an unresolved point source if the restriction is caused by an external screen, e.g., a dusty torus on

scales much larger than the accretion disk. But here we consider thick accretion disk models that have highly angle-dependent radiation fields. This is evident for Madau’s radiation model in Figure 5, with its footprint on the halo ionizing field shown in Figure 4. Here the obscuring torus has a half-opening angle $\theta_T = 30^\circ$; the accretion disk isophotes are seen to taper at $\theta_A = 20^\circ$. Both of these values are illustrative and not well constrained by the present observations.

4.2. Time-dependent Analytical Model of H Recombination

Thus far, we have assumed that some finite depth on the outer surface of a distant gas cloud comes into ionization equilibrium with the impinging radiation field. But what if the source of the ionizing radiation fades with time, consistent with the low Eddington fraction inferred today in the vicinity of Sgr A*? Then the ionization rate will decrease from the initial value for which equilibrium was established. We can treat the time dependence of the H recombination lines analytically (BH2013); due to the presence of metal-line cooling, the C and Si ions require a more complex treatment with the time-dependent *Mappings V* code. This analysis is covered in the next section, where we find, in fact, that the H α and UV diagnostics arise in different regions of the Magellanic Stream.

After Sharp & Bland-Hawthorn (2010), we assume an exponential decline for φ_i , with a characteristic timescale for the ionizing source τ_s . The time-dependent equation for the electron fraction $x_e = n_e/n_H$ is

$$\frac{dx_e}{dt} = -\alpha n_H x_e^2 + \zeta_0 e^{-t/\tau_s} (1 - x_e), \quad (8)$$

where ζ is the ionization rate per atom. This was solved for in BH2013 (Appendix A). If we let $\tau_s \rightarrow 0$, so that φ_i declines instantaneously to zero, we are left with

$$\frac{dx_e}{dt} = -\alpha n_H x_e^2. \quad (9)$$

For the initial condition $x_e = 1$ at $t = 0$, we get

$$x_e = (1 + t/\tau_{\text{rec}})^{-1}, \quad (10)$$

for which the recombination time $\tau_{\text{rec}} = 1/\alpha n_H$ and $\alpha_B = 2.6 \times 10^{-13} \text{ cm}^3 \text{ s}^{-1}$ for the recombination coefficient (appropriate for hydrogen at 10^4 K). Thus, the emission measure

$$\mathcal{E}_m = 1.25 \varphi_6 x_e^2(t) \text{ cm}^{-6} \text{ pc}, \quad (11)$$

where φ_6 is the ionizing photon flux in units of $10^6 \text{ photons cm}^{-2} \text{ s}^{-1}$. It follows from Equation (7) that

$$\begin{aligned} \mu_*(t) &= 440 \left(\frac{f_E}{0.1} \right) \left(\frac{f_{*,\text{esc}}}{1.0} \right) \\ &\times \left(\frac{D}{75 \text{ kpc}} \right)^{-2} (1 + t/\tau_{\text{rec}})^{-2} \text{ mR}. \end{aligned} \quad (12)$$

Equations (7) and (12) have several important implications. Note that the peak brightness of the emission depends only on the AGN parameters and the Magellanic Stream distance, not the local conditions within the Magellanic Stream. (This assumes that the gas column density is large enough to absorb all of the incident ionizing flux, a point we return to in Section 4.3.) Hence, in our flare model, the Magellanic Stream gas just before the ionizing photon flux switches off may not be uniform in density or column density, but it would appear uniformly bright in H α . After the ionizing source turns off, this ceases to be true: the highest-density regions fade first, because they have the shortest recombination times; the differential fading scales as $1/(1 + t/\tau_{\text{rec}})^2$. This is clearly seen in BH2013 (Figure 6), which shows the H α surface brightness versus n_e for fixed times after the flare has ended: at any given time, it is the lowest-density gas that has the brightest H α

emission, even as all of the Magellanic Stream is decreasing in brightness.

In Figure 7, we show two sets of three fading curves defined by two values of f_E , 0.1 and 1, the range suggested by most AGN models of the X-ray/ γ ray bubbles (e.g., Guo & Mathews 2012), although higher super-Eddington values have been proposed (e.g., Zubovas & Nayakshin 2012). The three curves cover the most likely range of cloud density n_H (derived in the next section). The model sets overlap for different combinations of f_E and n_H . The hatched horizontal band is the median H α surface brightness over the SGP as discussed in BH2013. The horizontal axis is the elapsed time since the Seyfert flare event.

The red tracks are reasonable models that explain the H α emission, and these all fall within the red hatched region. The denser hatching in blue is a more restricted duration to explain the C IV/C II values at the SGP (Section 4.4). With the UV diagnostic constraints from *HST*, we find that $\log u_o \sim -3$ is a reasonable estimate of the initial ionization parameter that gave rise to the H α emission we see today. In Figure 8, we see that a *continuous* radiation field fixed at u_o can produce the UV diagnostics observed, but such models require very large HI column densities (Section 4.3). This situation is unrealistic given the weak AGN activity observed today. Thus, to accommodate the fading intensity of the source, we must start at a much higher u to account for the UV diagnostics. Below, we find that the observed C and Si absorption lines are unlikely to arise from the same gas that produces H α .

4.3. Critical Column Density Associated with Flare Ionization

We have assumed until now that the Magellanic Stream has sufficient hydrogen everywhere within the observed solid angle to absorb the ionizing UV radiation from the Seyfert nucleus (e.g., Nidever et al. 2008). For a continuous source of radiation (e.g., Figure 8), this requires an H column density greater than a critical column density N_{cr} given by

$$N_{\text{cr}} \approx 3.9 \times 10^{19} \phi_6 (\langle n_H \rangle / 0.1)^{-1} \text{ cm}^{-2}, \quad (13)$$

where ϕ_6 is the ionizing UV luminosity in units of $10^6 \text{ photons cm}^{-2} \text{ s}^{-1}$. For simplicity, we set $D = 75 \text{ kpc}$ and $f_{\text{esc}} = 1$. By substituting from Equation (6), we find

$$N_{\text{cr}} \approx 4.2 \times 10^{20} (f_E/0.1) (\langle n_H \rangle / 0.1)^{-1} \text{ cm}^{-2}, \quad (14)$$

where f_E is the Eddington fraction and $\langle n_H \rangle$ is the local hydrogen volume density in units of cm^{-3} . Thus,

$$N_{\text{cr}} \approx 1 \times 10^{20} u_{-3} \text{ cm}^{-2}, \quad (15)$$

where u_{-3} is the ionization parameter in units of 10^{-3} , consistent with Figure 7, and where it follows

$$u_{-3} = 0.37 (f_E/0.1) (\langle n_H \rangle / 0.1)^{-1}. \quad (16)$$

Barger et al. (2017, Figure 12) plot the HI column densities (averaged over the same 1° beam as their WHAM H α observations) versus the H α intensity. The measured values suggest that the total HI column may fall below that set by Equation (14) except in high-density regions ($\langle n_H \rangle \geq 1$). In this case, the peak H α surface brightness will be reduced by a factor $\sim N_H/N_{\text{cr}}$ from the value predicted by Equation (7). This will contribute to, and could even dominate (see Section 4.8.1), the spread in the observed $\mu(\text{H}\alpha)$. For lines of sight with

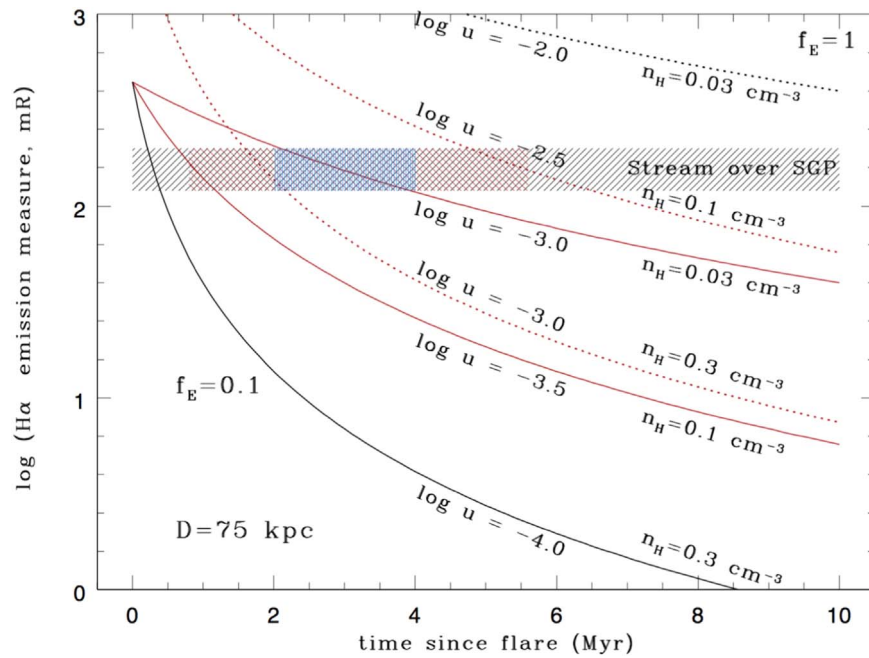


Figure 7. Decline in the $H\alpha$ surface brightness with time since the Seyfert flare event for gas clouds at a distance of $D = 75$ kpc. The event ends abruptly in time at zero, and the recombination signal declines depending on the cloud density. The light-travel time there and back (roughly 0.5 Myr; BH2013) is not included here. Three tracks are shown (solid lines) for an Eddington fraction $f_E = 0.1$ representing gas ionized at three different densities (0.03 – 0.3 cm^{-3}). The dotted lines show three tracks for an Eddington fraction of $f_E = 1$. The value of the ionization parameter is shown at the time of the flare event. The hatched horizontal band is the observed $H\alpha$ surface brightness over the SGP. The red tracks are plausible models that explain the $H\alpha$ emission, and these all fall within the red hatched region. The denser hatching in blue is a shorter duration fully consistent with timescales derived from the UV diagnostics (see text). Consistency between the independent diagnostics argues for $\log u = -3$ (independent of f_E) as characteristic of the $H\alpha$ emission along the Magellanic Stream.

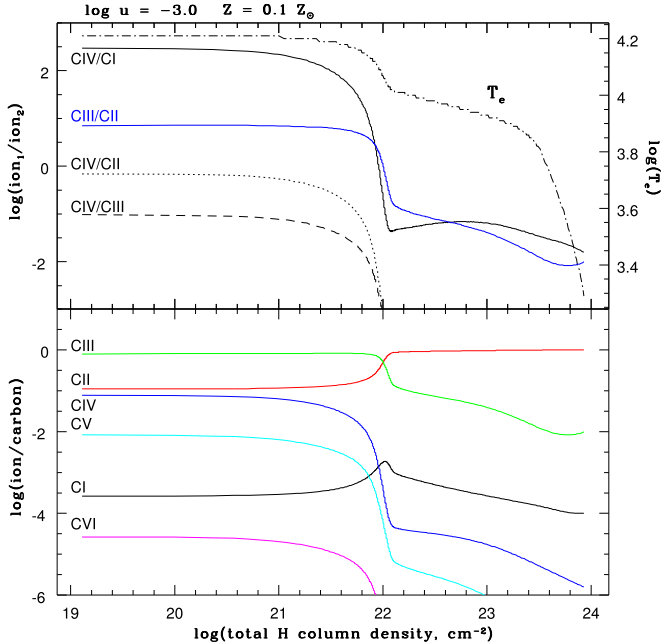


Figure 8. *Mappings V* ionization calculation for a continuously radiating power-law source in Figure 10(e) ($\alpha = -1$). At the front face, the radiation hits a cold slab of gas with subsolar metallicity ($Z = 0.1Z_\odot$) and ionization parameter $\log u = -3.0$. In the top panel, the change in the log ratio of two carbon (C) ions is shown as a function of depth into the slab. The log column densities on the horizontal axis are total H densities ($\text{H I} + \text{H}^+$) and are much larger than for the fading models. The dotted–dashed line is the electron temperature T_e of the gas as a function of depth, as indicated by the right-hand axis. The bottom panel shows the log ratio of each C ion to the total carbon content as a function of depth. The C IV/C II model track is to be compared to the data points in Figure 9.

$N_H > N_{\text{cr}}$, there is a constant “ionized column” recombination rate, balancing the incident ionizing flux. At the time of the Seyfert flash, once ionization equilibrium is reached (note that Equations (13)–(16) only apply when the central source is switched on), regions of lower gas density will extend deeper along the line of sight (and hence to larger N_p) to compensate for the lower $\langle n_e \rangle$.

4.4. Time-dependent Mappings Model of C, Si Recombination

We use the *Mappings V* code (Sutherland & Dopita 2017) to study the ionization, recombination, and cooling of the C and Si ions at the surface of Magellanic Stream clouds. To determine the expected column depths of the different ionization states, we explore a broad range of *Mappings V* photoionization models extending across black hole accretion disk, starburst, and individual stellar sources. The full range of models is illustrated in Figure 10. The vertical dashed lines at 13.6 and 64.5 eV⁸ delimit the most important energy range in the production of the H, Si, and C ions in our study.

For both the AGN and starburst/stellar photoionization models, we assume (i) a constant-density ionization-bounded slab with $n_H = 0.01$ cm^{-3} , (ii) a gas-phase metallicity of $Z = 0.1Z_\odot$ (Fox et al. 2013) made consistent for all elements with concordance abundances (Asplund 2005), (iii) that at these low metallicities we can ignore depletion onto dust grains, and (iv) that the gas column density is large enough everywhere to absorb all of the incident ionizing flux (Section 4.3). The results are only weakly dependent on n_H but have a strong dependence on the ionization parameter

⁸ The C IV ionization potential is 47.9 eV, but C v at 64.5 eV is important for reducing C IV in the presence of a hard ionizing continuum.

Table 1

Photoionization Models: Initial Conditions in the Gas Slab when the Ionizing Source Is Switched On

| Model | $\log u$ | Initial T_e | $N(\text{H}^+)$ | $N(\text{H I})$ |
|-------------------------|----------|-----------------|-----------------|-----------------|
| BLS (a) | -1.0 | 2.99E+04 | 3.08E+19 | 1.32E+15 |
| | -2.0 | 2.13E+04 | 3.08E+19 | 1.72E+16 |
| | -3.0 | <i>1.57E+04</i> | 3.05E+19 | 2.59E+17 |
| BLS + soft Compton (a) | -1.0 | 3.50E+04 | 3.08E+19 | 1.24E+15 |
| | -2.0 | 2.31E+04 | 3.08E+19 | 1.73E+16 |
| | -3.0 | <i>1.63E+04</i> | 3.05E+19 | 2.82E+17 |
| NLS (b) | -1.0 | 3.26E+04 | 3.08E+19 | 1.59E+15 |
| | -2.0 | 2.26E+04 | 3.08E+19 | 2.12E+16 |
| | -3.0 | <i>1.61E+04</i> | 3.05E+19 | 3.49E+17 |
| NLS + soft Compton (b) | -1.0 | 3.67E+04 | 3.08E+19 | 1.38E+15 |
| | -2.0 | 2.35E+04 | 3.08E+19 | 1.99E+16 |
| | -3.0 | <i>1.63E+04</i> | 3.05E+19 | 3.39E+17 |
| BH2013 (c) | -1.0 | 3.18E+04 | 3.08E+19 | 1.26E+15 |
| | -2.0 | 2.24E+04 | 3.08E+19 | 1.65E+16 |
| | -3.0 | <i>1.61E+04</i> | 3.05E+19 | 2.60E+17 |
| Star cluster (d) | -1.0 | <i>1.55E+04</i> | 3.08E+19 | 1.14E+15 |
| | -2.0 | <i>1.50E+04</i> | 3.08E+19 | 1.17E+16 |
| | -3.0 | <i>1.36E+04</i> | 3.07E+19 | 1.49E+17 |
| PL, $\alpha = -1.0$ (e) | -1.0 | 4.11E+04 | 3.08E+19 | 9.69E+14 |
| | -2.0 | 2.43E+04 | 3.08E+19 | 1.50E+16 |
| | -3.0 | <i>1.65E+04</i> | 3.06E+19 | 2.55E+17 |
| PL, $\alpha = -1.5$ (e) | -1.0 | 3.45E+04 | 3.08E+19 | 8.71E+14 |
| | -2.0 | 2.31E+04 | 3.08E+19 | 1.19E+16 |
| | -3.0 | <i>1.62E+04</i> | 3.06E+19 | 1.87E+17 |
| PL, $\alpha = -2.0$ (e) | -1.0 | 3.03E+04 | 3.08E+19 | 8.16E+14 |
| | -2.0 | 2.17E+04 | 3.08E+19 | 1.05E+16 |
| | -3.0 | <i>1.55E+04</i> | 3.06E+19 | 1.59E+17 |
| ULX100 (f) | -1.0 | 3.70E+04 | 3.08E+19 | 7.49E+15 |
| | -2.0 | 2.07E+04 | 3.07E+19 | 1.47E+17 |
| | -3.0 | <i>1.43E+04</i> | 2.50E+19 | 5.80E+18 |
| ULX1000 (f) | -1.0 | 4.00E+04 | 3.08E+19 | 4.55E+15 |
| | -2.0 | 2.19E+04 | 3.07E+19 | 8.83E+16 |
| | -3.0 | <i>1.50E+04</i> | 2.73E+19 | 3.48E+18 |
| 40,000 K Star (g) | -1.0 | <i>1.53E+04</i> | 3.08E+19 | 1.13E+15 |
| | -2.0 | <i>1.49E+04</i> | 3.08E+19 | 1.16E+16 |
| | -3.0 | <i>1.36E+04</i> | 3.07E+19 | 1.48E+17 |

Note. We consider the internal ionization structure to be instantaneous ($\ll 1$ Myr) because the ionization front propagates rapidly into the slab (BH2013). Column (1): ionizing source in Figure 10. Column (2): ionization parameter. Column (3): initial electron temperature. Column (4): ionized H column density. Column (5): neutral H column density. The temperatures in italics produce instantaneous highly ionized C and Si in the flash but are too low to produce sustained high ion ratios when the source fades. The predicted C and Si ion columns are given in Appendix B.

$u = \varphi/(cn_H) = 10^6 \varphi_6/(cn_H)$, which is how we choose to discuss the main results.

The setup for all photoionization models is given in Table 1, where the required ionized and neutral column densities are listed in Columns (4) and (5), respectively. In Column (3), we show the instantaneous electron temperature T_e after the flash occurs; values indicated in italics are generally too low for sustained enhancements in all of the UV diagnostics (ion ratios, column densities, etc.). We explore each of the models below, but, in summary, we find that for a fading source only the accretion-disk-driven radiation fields at high ionization parameter ($\log u \gtrsim -2$) generate the high temperatures required to

reproduce the observed UV diagnostics. We show illustrative plots for each diagnostic below, but the results are tabulated in Appendix B (Tables 2–3).

4.4.1. Stellar, Starburst, and ULX Models

In Figure 11 (top), even though star-forming regions in either the LMC or the Galaxy do not contribute significantly to the ionization of the Magellanic Stream, for completeness we include a *Mappings V* time-dependent ionization calculation for the fading star cluster model in Figure 10(d). We present the evolution of the Si IV/Si II and C IV/C II ratio (left) and the evolution in projected column density of H I and all four metal ions (right). The gray horizontal band encloses most of the data points along the Magellanic Stream (Fox et al. 2014). A comparison of both figures shows that the gas layer is cooling down through metal-line (and H) recombination. A stellar or starburst photoionizing spectrum fails to produce sufficient C IV or Si IV absorption (Tables 1–3), regardless of its bolometric luminosity.

For the incident ionizing radiation field, we also explore the CMFGEN O-star grid of Hillier (2012) and settle on an O star with $T_{\text{eff}} = 41,000$ K and $\log g = 3.75$, which represents a somewhat harder version of the typical Milky Way O star. Importantly, this ionizing spectrum is unable to excite appreciable amounts of C IV or Si IV. The same holds true for static photoionization models. Lower u values ($\log u < -2.0$) and stellar photoionization both fall short of producing such high columns and column ratios that, taken together, are a serious challenge for any model. Typical C IV columns from the hard stellar spectra rarely exceed 10^{10} cm^{-2} for a reasonable range of u .

But there is a special case we need to consider that is not factored into the existing Starburst99 models. ULXs are known to be associated with vigorous star-forming regions, and, indeed, a few have been observed in the LMC (Kaaret et al. 2017). In Figure 11, we show that the hard spectrum of the ULX source can in principle achieve the observed UV diagnostics along the Magellanic Stream. We do not believe that one or more ULX sources account for the enhanced values over the SGP, although they could account for the slightly elevated levels observed near the LMC (Figure 9). There are numerous problems with an LMC explanation as has been explored in earlier work. Barger et al. (2013) show that the mutual ionization of the LMC and SMC on their local gas is well established, as are their respective orientations. The $\text{H}\alpha$ surface brightness declines with radius for both sources. Furthermore, the C IV/C II and Si IV/Si II ratios rise dramatically as we move away from the LMC in Magellanic longitude ℓ_M (Figure 9), which is entirely inconsistent for the LMC being responsible. The extent of the LMC ionization is illustrated in Figure 3.

4.4.2. AGN Models

The bursty stellar ionizing radiation from the LMC or from the Galaxy fails by two orders of magnitude to explain the Magellanic Stream (BH2013, Appendix B). We believe that the most reasonable explanation is the fading radiation field of a Seyfert flare event. In Figure 7, the incident AGN radiation field strength is defined in terms of the initial ionization parameter u , and we explore three tracks that encompass the range expected across the Magellanic Stream: $\log u = -3.5$,

Table 2
Photoionization Models: Initial Conditions in the Gas Slab When the Ionizing Source Is Switched On

| Model | $\log u$ | T_e | $N(\text{C VII})$ | $N(\text{C VI})$ | $N(\text{C V})$ | $N(\text{C IV})$ | $N(\text{C III})$ | $N(\text{C II})$ |
|-------------------------|----------|-----------|-------------------|------------------|-----------------|------------------|-------------------|------------------|
| BLS (a) | -1.0 | 2.99E+04 | 1.82E+12 | 8.32E+13 | 6.86E+14 | 5.23E+13 | 5.21E+12 | 9.79E+09 |
| | -2.0 | 2.13E+04 | 4.50E+09 | 2.55E+12 | 2.64E+14 | 3.21E+14 | 2.39E+14 | 2.57E+12 |
| | -3.0 | 1.57E+04 | 1.43E+05 | 1.14E+09 | 1.40E+12 | 4.74E+13 | 7.09E+14 | 7.10E+13 |
| BLS + soft Compton (a) | -1.0 | 3.50E+04 | 1.29E+13 | 2.23E+14 | 5.75E+14 | 1.68E+13 | 1.38E+12 | 3.81E+09 |
| | -2.0 | 2.31E+04 | 5.99E+10 | 1.35E+13 | 4.60E+14 | 2.24E+14 | 1.30E+14 | 1.70E+12 |
| | -3.0 | 1.63E+04 | 3.85E+06 | 1.06E+10 | 4.46E+12 | 6.31E+13 | 6.86E+14 | 7.50E+13 |
| NLS (b) | -1.0 | 3.26E+04 | 1.49E+12 | 8.09E+13 | 7.29E+14 | 1.66E+13 | 9.14E+11 | 1.99E+09 |
| | -2.0 | 2.26E+04 | 6.72E+09 | 4.63E+12 | 5.34E+14 | 2.06E+14 | 8.38E+13 | 9.53E+11 |
| | -3.0 | 1.61E+04 | 3.72E+05 | 3.12E+09 | 4.42E+12 | 7.94E+13 | 6.77E+14 | 6.74E+13 |
| NLS + soft Compton (b) | -1.0 | 3.67E+04 | 1.84E+13 | 2.68E+14 | 5.32E+14 | 9.82E+12 | 6.28E+11 | 1.92E+09 |
| | -2.0 | 2.35E+04 | 1.06E+11 | 2.05E+13 | 5.49E+14 | 1.78E+14 | 8.00E+13 | 1.08E+12 |
| | -3.0 | 1.63E+04 | 8.14E+06 | 1.96E+10 | 6.55E+12 | 7.58E+13 | 6.71E+14 | 7.51E+13 |
| BH2013 (c) | -1.0 | 3.18E+04 | 6.02E+11 | 5.03E+13 | 7.48E+14 | 2.76E+13 | 2.24E+12 | 5.16E+09 |
| | -2.0 | 2.24E+04 | 2.15E+09 | 2.25E+12 | 4.23E+14 | 2.51E+14 | 1.51E+14 | 1.88E+12 |
| | -3.0 | 1.61E+04 | 7.24E+04 | 1.12E+09 | 2.57E+12 | 6.14E+13 | 6.90E+14 | 7.50E+13 |
| Star cluster (d) | -1.0 | 1.55E+04 | ... | ... | 1.07E+10 | 2.83E+14 | 5.45E+14 | 1.24E+12 |
| | -2.0 | 1.50E+04 | ... | ... | 1.21E+08 | 3.81E+13 | 7.73E+14 | 1.78E+13 |
| | -3.0 | 1.36E+04 | ... | ... | 2.67E+05 | 1.83E+12 | 6.53E+14 | 1.74E+14 |
| PL, $\alpha = -1.0$ (e) | -1.0 | 4.11E+04 | 1.34E+14 | 4.40E+14 | 2.49E+14 | 5.41E+12 | 5.41E+11 | 2.48E+09 |
| | -2.0 | 2.43E+04 | 1.28E+12 | 5.93E+13 | 4.77E+14 | 1.73E+14 | 1.17E+14 | 2.08E+12 |
| | -3.0 | 1.65E+04 | 1.71E+08 | 9.92E+10 | 1.01E+13 | 5.94E+13 | 6.67E+14 | 9.20E+13 |
| PL, $\alpha = -1.5$ (e) | -1.0 | 3.45E+04 | 1.30E+13 | 2.19E+14 | 5.68E+14 | 2.57E+13 | 3.51E+12 | 1.32E+10 |
| | -2.0 | 2.31E+04 | 4.74E+10 | 1.03E+13 | 3.47E+14 | 2.37E+14 | 2.30E+14 | 4.20E+12 |
| | -3.0 | 1.62E+04 | 3.45E+06 | 9.12E+09 | 3.81E+12 | 4.41E+13 | 6.79E+14 | 1.02E+14 |
| PL, $\alpha = -2.0$ (e) | -1.0 | 3.025E+04 | 5.902E+11 | 5.411E+13 | 6.936E+14 | 6.714E+13 | 1.349E+13 | 4.77E+10 |
| | -2.0 | 2.167E+04 | 9.969E+08 | 1.126E+12 | 1.794E+14 | 2.555E+14 | 3.853E+14 | 7.76E+12 |
| | -3.0 | 1.552E+04 | 8.440E+03 | 5.755E+08 | 1.109E+12 | 2.762E+13 | 6.764E+14 | 1.24E+14 |
| ULX100 (f) | -1.0 | 3.70E+04 | 6.49E+14 | 1.70E+14 | 9.38E+12 | 1.06E+11 | 8.14E+09 | 7.42E+07 |
| | -2.0 | 2.07E+04 | 8.62E+13 | 3.29E+14 | 2.67E+14 | 8.64E+13 | 5.87E+13 | 2.01E+12 |
| | -3.0 | 1.43E+04 | 1.20E+10 | 5.05E+11 | 4.60E+12 | 8.41E+10 | 5.75E+14 | 2.34E+14 |
| ULX1000 (f) | -1.0 | 4.00E+04 | 6.40E+14 | 1.80E+14 | 9.80E+12 | 9.01E+10 | 6.20E+09 | 5.12E+07 |
| | -2.0 | 2.19E+04 | 8.52E+13 | 3.52E+14 | 2.88E+14 | 6.73E+13 | 3.51E+13 | 1.02E+12 |
| | -3.0 | 1.50E+04 | 1.71E+10 | 8.43E+11 | 8.30E+12 | 1.61E+13 | 6.12E+14 | 1.89E+14 |
| 40,000 K Star (g) | -1.0 | 1.527E+04 | ... | ... | 2.391E+03 | 5.526E+12 | 8.217E+14 | 1.80E+12 |
| | -2.0 | 1.489E+04 | ... | ... | ... | 5.158E+11 | 8.104E+14 | 1.81E+13 |
| | -3.0 | 1.356E+04 | ... | ... | ... | 2.403E+10 | 6.584E+14 | 1.70E+14 |

Note. Column (1): ionizing source in Figure 10. Column (2): ionization parameter. Column (3): initial electron temperature. The remaining columns give predicted column densities for C ions as indicated.

-3.0, and -2.5. As argued in Section 4.2, this range can account for the Magellanic Stream $H\alpha$ emissivity, but the UV signatures likely arise under different conditions. We now investigate the C and Si diagnostics because of their potential to provide an independent estimate of when the Seyfert flare occurred.

Here, we explore a wide range of models summarized in Figure 10, including generic models of Seyfert galaxies, power-law spectra, and the ionizing Seyfert spectrum that includes a “big blue bump” based on the BH2013 model (Appendix C within), where we assumed a hot component (power-law) fraction of 10% relative to the big blue bump ($k_2 = k_1$ in Equation (3) of BH2013).

The time-dependent models were run by turning on the source of ionization, waiting for the gas to reach ionization/thermal equilibrium, and then turning off the ionizing photon flux. The sound-crossing time of the warm ionized layers is too long ($\gtrsim 10$ Myr) in the low-density regime relevant to our study

for isobaric conditions to prevail; essentially all of our results are in the isochoric limit.

We provide a synopsis of our extensive modeling in Figure 12 and Table 1. In order to account for the Si and C ion ratios and projected column densities, we must “over-ionize” the gas, at least initially. This pushes us to a higher-impact ionization parameter at the front of the slab. Given that the fading source must also account for the $H\alpha$ emissivity along the Magellanic Stream, we can achieve the higher values of u , specifically $\log u > -3$, by considering gas at even lower density ($\langle n_H \rangle < 0.01 \text{ cm}^{-3}$) consistent with the Magellanic Stream’s properties. Specifically, for the UV diagnostic sight lines, the HI column is in the range $\log = 17.8\text{--}18.3$ when detected (Fox et al. 2014, Figure 4), although for most sight lines only an upper limit in that range is possible. For our canonical Magellanic Stream depth of $L \sim 1$ kpc, this leads to $\langle n_H \rangle \sim 0.001 \text{ cm}^{-3}$. Such low densities lead to initially higher gas temperatures and slower cool-down and recombination rates.

Table 3
Photoionization Models: Initial Conditions in the Gas Slab When the Ionizing Source Is Switched On

| Model | $\log u$ | T_e | $N(\text{Si VII})$ | $N(\text{Si VI})$ | $N(\text{Si V})$ | $N(\text{Si IV})$ | $N(\text{Si III})$ | $N(\text{Si II})$ |
|-------------------------|----------|----------|--------------------|-------------------|------------------|-------------------|--------------------|-------------------|
| BLS (a) | -1.0 | 2.99E+04 | 3.61E+13 | 4.36E+13 | 1.34E+13 | 3.29E+11 | 5.92E+10 | 7.36E+08 |
| | -2.0 | 2.13E+04 | 7.47E+11 | 1.09E+13 | 4.33E+13 | 2.27E+13 | 2.12E+13 | 7.84E+11 |
| | -3.0 | 1.57E+04 | 9.66E+07 | 1.36E+10 | 6.25E+11 | 1.23E+13 | 7.02E+13 | 1.65E+13 |
| BLS + soft Compton (a) | -1.0 | 3.50E+04 | 4.85E+13 | 1.09E+13 | 5.05E+11 | 3.96E+09 | 4.92E+08 | 6.72E+06 |
| | -2.0 | 2.31E+04 | 1.60E+13 | 4.59E+13 | 2.90E+13 | 4.73E+12 | 2.90E+12 | 1.10E+11 |
| | -3.0 | 1.63E+04 | 1.14E+10 | 4.03E+11 | 3.30E+12 | 2.00E+13 | 6.14E+13 | 1.45E+13 |
| NLS (b) | -1.0 | 3.26E+04 | 4.22E+13 | 4.17E+13 | 7.82E+12 | 9.68E+10 | 1.26E+10 | 1.67E+08 |
| | -2.0 | 2.26E+04 | 1.69E+12 | 2.08E+13 | 5.13E+13 | 1.52E+13 | 1.03E+13 | 4.00E+11 |
| | -3.0 | 1.61E+04 | 2.85E+08 | 4.08E+10 | 1.28E+12 | 1.68E+13 | 6.33E+13 | 1.81E+13 |
| NLS + soft Compton (b) | -1.0 | 3.67E+04 | 4.20E+13 | 6.25E+12 | 1.85E+11 | 9.93E+08 | 9.68E+07 | 0 |
| | -2.0 | 2.35E+04 | 2.52E+13 | 4.86E+13 | 1.99E+13 | 2.57E+12 | 1.20E+12 | 4.51E+10 |
| | -3.0 | 1.63E+04 | 3.26E+10 | 7.93E+11 | 4.28E+12 | 2.46E+13 | 5.50E+13 | 1.49E+13 |
| BH2013 (c) | -1.0 | 3.18E+04 | 3.21E+13 | 5.10E+13 | 1.30E+13 | 2.15E+11 | 3.54E+10 | 4.70E+08 |
| | -2.0 | 2.24E+04 | 8.02E+11 | 1.56E+13 | 5.16E+13 | 1.66E+13 | 1.45E+13 | 5.52E+11 |
| | -3.0 | 1.61E+04 | 1.47E+08 | 3.07E+10 | 1.28E+12 | 1.43E+13 | 6.84E+13 | 1.55E+13 |
| Star cluster (d) | -1.0 | 1.55E+04 | ... | ... | 3.86E+13 | 4.17E+13 | 1.93E+13 | 9.85E+10 |
| | -2.0 | 1.50E+04 | ... | ... | 1.03E+12 | 1.79E+13 | 7.82E+13 | 2.60E+12 |
| | -3.0 | 1.36E+04 | ... | ... | 1.86E+09 | 1.83E+12 | 8.14E+13 | 1.64E+13 |
| PL, $\alpha = -1.0$ (e) | -1.0 | 4.11E+04 | 2.24E+13 | 1.74E+12 | 3.12E+10 | 1.30E+08 | 1.44E+07 | ... |
| | -2.0 | 2.43E+04 | 3.92E+13 | 4.07E+13 | 1.07E+13 | 9.84E+11 | 4.99E+11 | 1.90E+10 |
| | -3.0 | 1.65E+04 | 1.43E+11 | 1.87E+12 | 6.51E+12 | 2.45E+13 | 5.50E+13 | 1.17E+13 |
| PL, $\alpha = -1.5$ (e) | -1.0 | 3.45E+04 | 4.95E+13 | 1.28E+13 | 7.14E+11 | 7.07E+09 | 1.23E+09 | 1.82E+07 |
| | -2.0 | 2.31E+04 | 1.33E+13 | 4.34E+13 | 3.26E+13 | 4.98E+12 | 4.38E+12 | 1.68E+11 |
| | -3.0 | 1.62E+04 | 9.49E+09 | 3.82E+11 | 3.74E+12 | 1.60E+13 | 6.75E+13 | 1.20E+13 |
| PL, $\alpha = -2.0$ (e) | -1.0 | 3.03E+04 | 4.37E+13 | 4.04E+13 | 7.57E+12 | 1.78E+11 | 4.94E+10 | 7.01E+08 |
| | -2.0 | 2.17E+04 | 1.69E+12 | 1.92E+13 | 4.60E+13 | 1.30E+13 | 1.91E+13 | 7.23E+11 |
| | -3.0 | 1.55E+04 | 3.87E+08 | 5.34E+10 | 1.65E+12 | 9.78E+12 | 7.52E+13 | 1.30E+13 |
| ULX100 (f) | -1.0 | 3.70E+04 | 4.33E+11 | 6.05E+09 | 2.50E+07 | ... | ... | ... |
| | -2.0 | 2.07E+04 | 3.81E+13 | 7.52E+12 | 4.78E+11 | 1.03E+11 | 1.47E+10 | 9.11E+08 |
| | -3.0 | 1.43E+04 | 5.56E+11 | 1.24E+12 | 7.57E+11 | 2.22E+13 | 1.24E+13 | 6.19E+13 |
| ULX1000 (f) | -1.0 | 4.00E+04 | 4.31E+11 | 5.33E+09 | 1.87E+07 | ... | ... | ... |
| | -2.0 | 2.19E+04 | 3.68E+13 | 6.45E+12 | 3.51E+11 | 4.21E+10 | 5.86E+09 | 2.64E+08 |
| | -3.0 | 1.50E+04 | 1.30E+12 | 2.78E+12 | 1.88E+12 | 3.06E+13 | 1.70E+13 | 4.55E+13 |
| 40,000 K Star (g) Star | -1.0 | 1.53E+04 | 1.00E+00 | ... | 2.45E+12 | 6.51E+13 | 3.20E+13 | 1.67E+11 |
| | -2.0 | 1.49E+04 | 1.00E+00 | ... | 4.00E+10 | 1.70E+13 | 8.00E+13 | 2.70E+12 |
| | -3.0 | 1.36E+04 | 9.95E-01 | ... | 7.11E+07 | 1.70E+12 | 8.15E+13 | 1.64E+13 |

Note. Column (1): ionizing source in Figure 10. Column (2): ionization parameter. Column (3): initial electron temperature. The remaining columns give predicted column densities for Si ions as indicated.

The range of densities derived in this way is reasonable. The high end of the range explains the presence of both HI and H₂ in absorption along the Magellanic Stream (Richter et al. 2013). More generally, for a spherical cloud, its mass is approximately $M_c \sim f_n \rho_c d_c^3 / 2$, where the subscript n denotes that the filling factor refers to the neutral cloud prior to external ionization. From the projected HI and H α data combined, the Magellanic Stream clouds rarely exceed $d_c \approx 300$ pc in depth and $N_c \approx 10^{21}$ cm⁻² in column, indicating total gas densities of $n_H = \rho_c / m_p \lesssim$ a few atoms cm⁻³ in the densest regions, but extending to a low-density tail (reaching to 3 dex smaller values) for most of the projected gas distribution.

In Figure 12, we see that the higher ionization parameters (upper: $\log u = -1$, lower: $\log u = -2$) are ideal for reproducing the UV diagnostics (gray bands). The very high photon fluxes (relative to the adopted $\langle n_H \rangle \sim 0.001$ cm⁻³) generate high temperatures in the gas (~ 20 – $30,000$ K depending on

$\log u$; Table 1), and the harder spectrum ensures the higher ion columns (see Figure 8). This gas cools in time, creating enhanced amounts of lower ionization states like C II. The lower initial densities ensure that the cooling time is not too rapid. UV diagnostics like C IV/C II and Si IV/Si II decline on timescales of order a few megayears.

Note that AGN models run at higher u ($\log u > -1$) are unphysical within the context of our framework. This would either require even lower gas densities in the slab, which are inconsistent with the observed column densities in the Magellanic Stream, or an AGN source at Sgr A* that has super-Eddington accretion ($f_E > 1$). While such sources appear to exist around low-mass black holes (e.g., Kaaret et al. 2017), we are unaware of a compelling argument for super-Eddington accretion in Seyfert nuclei (see Begelman & Bland-Hawthorn 1997). In any event, going to an arbitrarily high u with a hard ionizing spectrum overproduces C v and higher states at the expense of C IV.

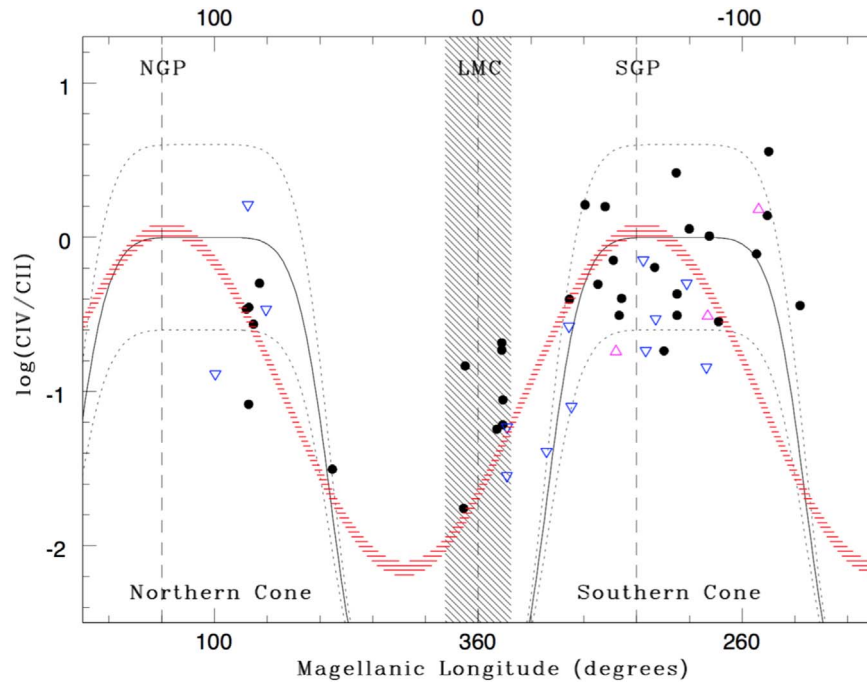


Figure 9. Column density ratio of C IV/C II (Fox et al. 2014) along the Magellanic leading arm (left of shaded band) and trailing Stream (right of shaded band) presented as a function of Magellanic longitude ℓ_M . Detections are shown as filled symbols, with typical 1σ errors being twice the size of the symbol; upper limits are shown as blue triangles, lower limits as magenta triangles. The NGP, LMC longitude, and SGP are all indicated as vertical long-dashed lines. The measured values within the shaded vertical band fall along the LMC sight line. The domain of the ionization cones (NGP and SGP; see Figure 2) is indicated by the two \cap -shaped curves; the dotted lines indicate ± 0.25 dex in $\log u$. The specific Madau accretion disk model used is discussed in Section 3. Note that some of the enhanced C IV/C II values—seen against the “leading arm” of the Magellanic Stream—fall within the NGP cone. The slightly elevated values in the LMC’s vicinity may be due to hard (e.g., ULX) ionizing sources within the dwarf galaxy. The red sinusoid (Section 5) is an attempt to force-fit the distribution of C IV/C II line ratios with spherical harmonics as a function of the sky coordinates.

4.5. Constraining the Look-back Time of the Seyfert Flash

If Sgr A* were radiating at close to the Eddington limit within the past 0.5 Myr, the entire Magellanic Stream over the SGP would be almost fully ionized (e.g., Figure 8)—this is not observed. Instead, we are witnessing the Magellanic Stream at a time when the central source has switched off and the gas is cooling down. The different ions (H, C II, Si II, C IV, Si IV) recombine and cool at different rates depending on the local gas conditions. We can exploit the relative line strengths to determine a unique timescale while keeping in mind that the observed diagnostics probably arise in more than one environment.

Taken together, the $H\alpha$ surface brightness and the UV diagnostic ratios observed along the Magellanic Stream tell a consistent story about the look-back time to the last major ionizing event from Sgr A* (see Figures 6, 7, 11). These timescales are inferred from detailed modeling, but the model parameters are well motivated. For a Magellanic Stream distance of 75 kpc or more, the Eddington fraction is in the range $0.1 < f_E < 1$. For our model to work, we require the $H\alpha$ emission and UV absorption lines to arise from different regions. For the same burst luminosity, the initial ionization parameter $u_o^{H\alpha}$ to account for the $H\alpha$ emission is $\log u_o^{H\alpha} \sim -3$ impinging on gas densities above $\langle n_H \rangle \sim 0.1 \text{ cm}^{-3}$. The initial conditions u_o^{UV} for the UV diagnostics are somewhat different, with $\log u_o^{UV} \sim -1$ to -2 operating with gas densities above $\langle n_H \rangle \sim 0.001 \text{ cm}^{-3}$.

In Figure 12, the AGN models are able to account for the UV diagnostics. The time span is indicated by when both the C IV/C II and Si IV/Si II tracks fall within the gray band

accommodating most of the “ionization cone” data points in Figure 9. The lower time limit is defined by $\log u = -2$ (both AGN model tracks in band) and the upper time limit by $\log u = -1$. Taken together, this indicates a look-back time for the AGN flash of about 2.5–4.5 Myr. As shown in Figure 7, the UV diagnostics are more restrictive than the $H\alpha$ constraint. When looking at both figures, we must include the double-crossing time of $2T_c \approx 0.5$ Myr (BH2013) to determine the total look-back time.

4.6. Fading Source: Rapid Cutoff or Slow Decay?

Our model assumption that the flare abruptly turned off is not necessarily correct, and the behavior of the $H\alpha$ emission and the UV diagnostics can be different when the flare decay time is nonzero. To understand this behavior, in Figure 13 we reproduce for the reader’s convenience Figure 8 from BH2013. This shows the $H\alpha$ surface brightness relative to the peak value as a function of τ , the time since the source’s flare began to decline in units of the recombination time. Each curve is labeled with the ratio of the recombination time to the e -folding timescale for the flare decay, τ_s . Note that the limiting case $\tau_{\text{rec}}/\tau_s = \infty$ is for a source that instantly turns off.

We refer the reader to Appendix A of BH2013 for mathematical details, but the important point is the following. If τ_{rec}/τ_s is small, say, 0.2, the surface brightness does not begin declining until $\tau \approx 20$. This is just a reflection of the fact that if the recombination time is short compared to the source decay time, the ionization equilibrium tracks the instantaneous incident ionizing photon flux, and the flare decline takes many recombination times. If τ_{rec}/τ_s is greater than roughly a few, on

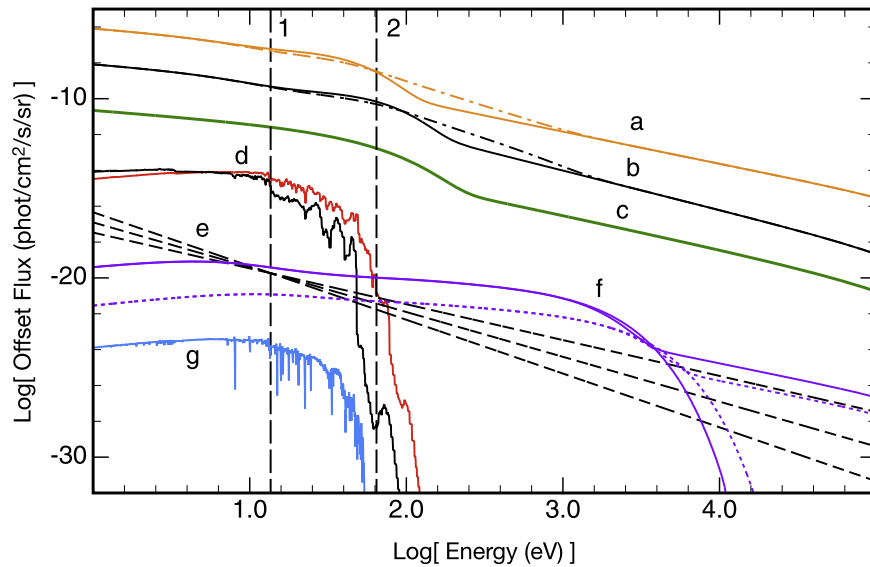


Figure 10. Broad distribution of ionizing continua explored within the current work using *Mappings V*. The offsets along the vertical axis are arbitrary: all model spectra are normalized to the same photon number in the window indicated by the vertical dashed lines (1, 2), important for the production of H, Si, and C ions. From top to bottom: generic (a) broad-line and (b) narrow-line Seyfert spectra from OPTXAGNF code (Done et al. 2012; Jin et al. 2012), where the dotted-dashed line includes a 0.2 keV “soft Compton” corona—both are scaled to M_* in Sgr A* ($R_c = 60R_g$, $f_{\text{PL}} = 0.4$, $\Gamma \approx 2$); (c) Seyfert spectrum derived by JBH2013 from NGC 1068 observations; (d) Starburst99 spectra for impulsive burst (red) and extended 4 Myr phase (black) assuming a Kroupa IMF; (e) power-law spectra with $f_i \propto \nu^\alpha$ for which $\alpha = -1.0, -1.5$, and -2.0 ; (f) a total of four ULX spectra from the OPTXAGNF code split between $M_* = 100 M_\odot$ (dotted line) and $M_* = 1000 M_\odot$ (solid line), both models with an inner disk ($R_c = 6R_g$), and one case each with an extended component ($R_c = 20R_g$, $f_{\text{PL}} = 0.2$, $\Gamma \approx 2$)—all models are fed for 1 Myr at $f_E = 1$; (g) hot star from the CMFGEN code with solar metallicity, surface temperature 41,000 K, and surface gravity $\log g = 3.75$ (Hillier 2012).

the other hand, then the results are nearly indistinguishable from the instant turnoff case, except for $\tau < 1$.

Although Figure 13 shows the normalized $H\alpha$ surface brightness, it applies to any measure of the ionization state of the gas, in particular to C IV/C II. In Figure 14, we use *Mappings V* to compute the time dependence of the relevant carbon ion ratios after the Magellanic Stream gas has been hit by a Seyfert flare. In this model the gas has been allowed to come into photoionization equilibrium, and then the source was turned off. Results are presented for two different ionization parameters, $\log u = -2.0, -3.0$. We scale out the density dependence by using $\langle n_{\text{H}} \rangle t$ as the horizontal axis. Note that this is equivalent to plotting time τ in recombination times, as in Figure 13.

This figure illustrates two important points. First, once C II becomes the dominant carbon ion, at $\log \langle n_{\text{H}} \rangle t \approx 4.4$, it has a recombination time that exceeds that of H^+ . Second, and more importantly for the Magellanic Stream UV absorption line observations, C IV is abundant only for a very limited range in $\log \langle n_{\text{H}} \rangle t$, due to its rapid recombination. Since the UV observations show that C IV and C II are comparable in abundance (see Figure 9), this places a strict upper limit on the age of the burst once the gas density is known. (Note that in the regime where the C IV/C II ratio is near the observed values, C III is the dominant carbon ion in the gas.)

For C IV, τ_{rec}/τ_s is always much smaller (for gas of similar density) than it is for H^+ ; this is why the C IV abundance declines so much more rapidly compared to H^+ in Figure 14. It is plausible that τ_{rec} for C IV is short compared to τ_s (indeed, this is the likely case unless the flare decay was very abrupt or the Magellanic Stream densities are unexpectedly low). Hence, the carbon ionization balance will closely track the photoionization equilibrium corresponding to the instantaneous value of ϕ (and hence u), while the $H\alpha$ emission will reflect an earlier, larger ionizing flux.

In summary, the flare could be decaying at the present look-back time of approximately half a million years, and the carbon absorption lines (in particular, C IV/C II) measure the strength of the ionizing flux at that time. The brightest $H\alpha$ emission then reflects the peak intensity of the ionizing flux, or at least something closer to that value than what is indicated by the carbon ion ratios.

4.7. Other Potential Sources of Ionization

4.7.1. Explosive Shock Signatures

We find that a *Fermi* bubble-like explosion in the distant past ($\sim 150 \text{ Myr}$ ($v_s/500 \text{ km s}^{-1}$) $^{-1}$)—moving through the Magellanic Stream today with a shock velocity v_s —cannot explain either the UV diagnostics or the $H\alpha$ emissivity, even considering the additional contribution from the photoionized precursor. The detailed modeling of Miller & Bregman (2016) makes that very clear when extrapolated from 10 kpc (tip of the bubble) to a distance of 75 kpc or more. The intrinsic wind velocity creating the pressure in the bubbles is of order 3000–10,000 km s^{-1} (Guo & Mathews 2012), but the wind must push aside the hot Galactic corona to reach the Magellanic Stream.

Today, there is a strong pressure gradient across the bubbles, with a thermal pressure (P_{th}/k) of roughly 6000 $\text{cm}^{-3} \text{ K}$ at the base dropping to about 1000 $\text{cm}^{-3} \text{ K}$ at the tip. The hot shell has an outflow (shock) velocity of $v_s \approx 490 \text{ km s}^{-1}$ (Mach number $\mathcal{M} \approx 2-3$) pushing into an external Galactic corona with $P/k \approx 200 \text{ cm}^{-3} \text{ K}$. If a cloud exists at the tip of the *Fermi* bubbles, the combined thermal and ram pressure shock driven into the lowest-density gas drives a shock velocity of $v_s \approx 60 \text{ km s}^{-1}$, too weak to account for C IV, Si IV, or the $H\alpha$ emissivity. The same holds true for the weak X-ray emission emanating from the cooling bubbles.

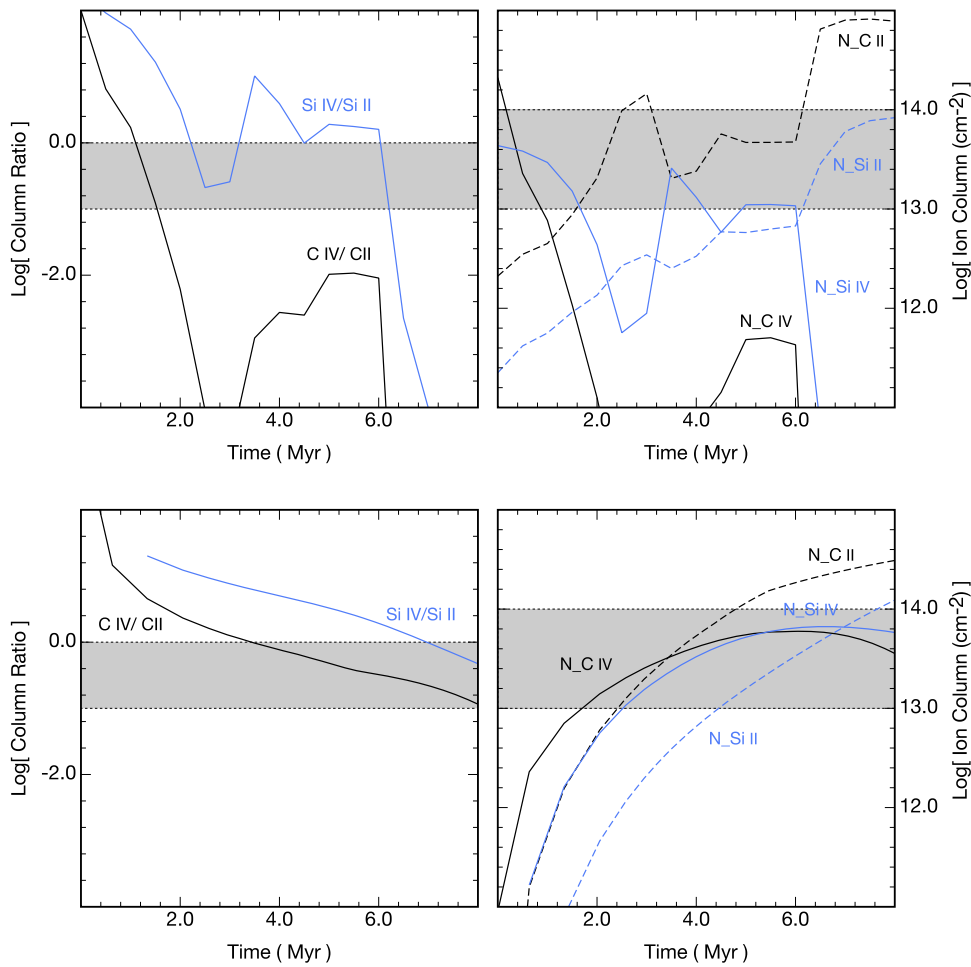


Figure 11. *Mappings V* time-dependent ionization calculation for the fading star cluster model in Figure 10(d) (top) and for the fading ULX model with the hardest spectrum in Figure 10(f) (bottom). Left: time evolution of the Si IV/Si II and C IV/C II ratios; right: projected column density of all four ions. The light travel time from source to Stream and back (0.5 Myr; BH2013) is not included here. The gray horizontal band encloses most of the high-ionization data points along the Magellanic Stream (Figure 9; Fox et al. 2014). A stellar or starburst, photoionizing spectrum fails to produce sufficient C IV or Si IV absorption regardless of its bolometric luminosity. In principle, a ULX spectrum can produce the observed UV diagnostic ratios and column densities; this may account for the enhanced C IV/C II localized around the LMC (Figure 9). The initial ionization parameter at the front face of the slab is $\log u_o = -1$ for both models ($Z = 0.1Z_\odot$). At $\log u_o = -2$, the tracks in the top figures fall below the gray band, and the tracks in the bottom figures cross the gray band in half the time. The results for more ions are presented in Appendix B.

In reality, the *Fermi* bubbles are expected to expand and diffuse into the Galactic corona after only a few tens of kiloparsecs, such that the hot shell never reaches the Magellanic Stream. To date, diffuse X-ray emission associated directly with the Magellanic Stream has never been observed and would not be expected in our scenario. Thus, we do *not* believe that an energetic bubble (or jet) has ever swept past the Magellanic Stream, and even if it were possible, the shock front would be too weak to leave its mark.

For completeness, we use *Mappings V* to explore plausible time-dependent shock scenarios for exciting C IV and Si IV. Once again, we treat metal-poor gas and assume a 1D planar geometry at the working surface. If the shock is allowed to run indefinitely, it cools down to a mostly neutral phase near 100 K. Under these conditions, C II and Si II ionization fractions steadily rise with respect to the higher ionization states. If we truncate the cooling shock at 10^4 K, C IV/C II and Si IV/Si II are both less than 0.1 for fast shocks ($v_s \gtrsim 100 \text{ km s}^{-1}$) but diverge for slow shocks, e.g., $v_s = 60 \text{ km s}^{-1}$ gives C IV/C II ≈ 0.01 and Si IV/Si II ≈ 25 . These are manifestly inconsistent with observations.

In Figure 15, we compute the C IV/C II and Si IV/Si II ion ratios versus the ionized gas temperature, T_e . This ratio is *not* independent of the gas abundances for metal-poor gas; the calculation is undertaken with $Z = 0.1Z_\odot$. The ion ratios reach parity at $T_e \approx 10^4$ K and for $T_e > 10^{5.3}$ K. Taken together, the ion ratios are certainly consistent with photoionization, but their convergence at higher temperature suggests another possible origin. The C IV/C II ratio, like the Si IV/Si II ratio (both with up to 0.5 dex of scatter), is of order unity and is enhanced in a region over the SGP and NGP (see Figure 9). So are there other ways to increase the gas temperature without photoionization or shocks from blast waves? We address this issue in the next section.

4.7.2. Shock Cascade and Turbulent Mixing

Bland-Hawthorn et al. (2007) and Tepper-Garcia et al. (2015) consider the case of the Magellanic H I stream being ablated by the diffuse hot halo. They show that the post-shock cooling gas ($v_s < 20 \text{ km s}^{-1}$) in a “shock cascade” is generally too weak along the Magellanic Stream to power the $H\alpha$

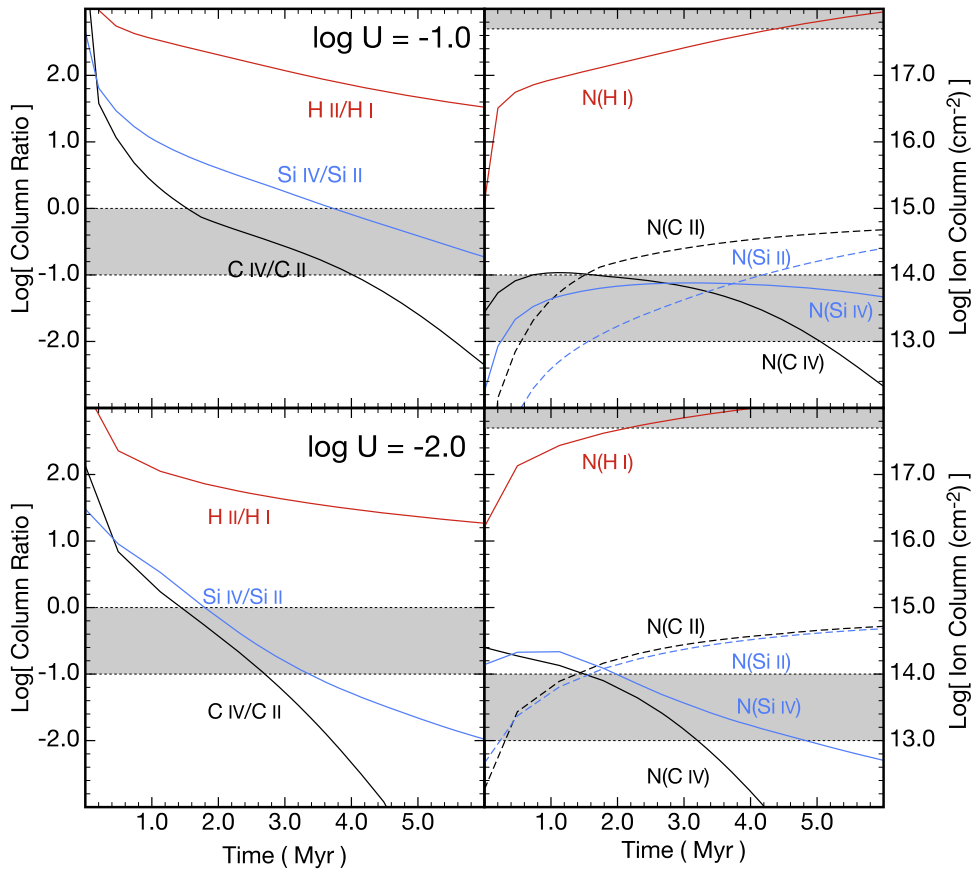


Figure 12. *Mappings V* time-dependent ionization calculation for the fading AGN model in Figure 10(c). The initial ionization parameter at the front face of the slab is $\log u_o = -1$ (top) and $\log u_o = -2$ (bottom) where $Z = 0.1Z_\odot$. In the left panels, the gray band refers to the observed C IV/C II and Si IV/Si II ratios; there is no UV constraint for H⁺/H I. The gray horizontal bands enclose most of the high-ionization data points along the Magellanic Stream (Figure 9; Fox et al. 2014). The AGN models considered (Table 1) give essentially the same results with only small differences in the trends. In the right panels, the evolution in projected column density is shown for four metal ions and H I determined from UV spectroscopy. The top gray band refers to H I, for which most values quoted in Fox et al. (2014) are upper limits; the bottom gray bands refers to the metal ions. For the tracks in the left panels to fall within the gray band simultaneously, over the allowed range of u_o ($-2 < \log u_o < -1$), the estimated time span is 2–4 Myr. The light travel time from source to Stream and back (0.5 Myr; BH2013) is not included here. The results for more ions are quantified in Appendix B.

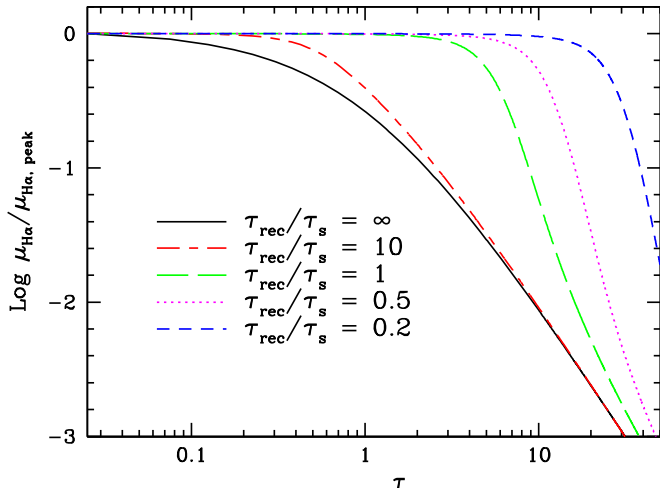


Figure 13. Predicted H α surface brightness relative to the peak value vs. time τ measured in units of the recombination time. The individual curves are labeled with the ratio of the recombination time τ_{rec} to the flare e -folding time, τ_s .

emission, particularly at the newly established distance of $D > 75$ kpc (see Barger et al. 2017). The post-shock temperature ($< 10^4$ K) is too low to produce high-ionization species, even in the high-energy tail of the particle distribution (see

Figure 15). But a shock cascade can still be important even if it does not account for the observed spectral signatures directly. For example, it can help to break down the cold gas and enable interchange with the hot halo.

A major uncertainty along the Magellanic Stream is the degree of mixing between the cold clouds and the hot coronal gas; a shearing boundary layer can give rise to intermediate gas phases with a mean temperature of order $\sqrt{T_{\text{hot}} T_{\text{cold}}}$ and therefore a broad range of ionization states (Begelman & Fabian 1990; Ji et al. 2019). This process is driven by either Kelvin–Helmholtz (KH) instabilities at the hot/cold interface or turbulence in the hot corona, for which there are few constraints currently. The outcome depends on the fraction of mass of hot gas deposited into the mixing layer and the efficiency of hydrodynamic mixing.

To our knowledge, there have only been two hydrodynamic studies of this turbulent regime that incorporate consistent nonequilibrium ionization, i.e., Esquivel et al. (2006; MHD) and Kwak & Shelton (2010; HD). Notably, Kwak & Shelton (2010) find, much like for conductive interfaces (see below), that the low and high ionization states arise from very low column gas ($\lesssim 10^{13} \text{ cm}^{-2}$). While mixing in sheared layers surely exists at the contact surface of the *Fermi* bubbles (Cooper et al. 2008; Gronke & Oh 2018), it is unclear whether

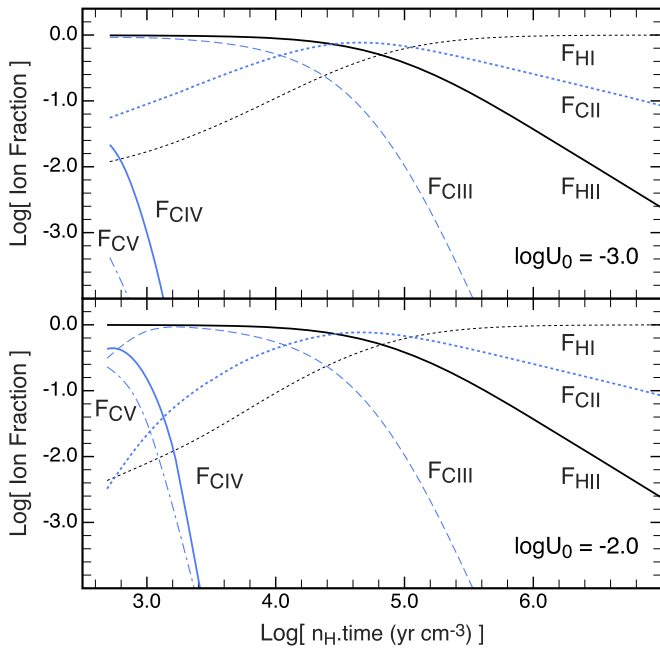


Figure 14. *Mappings V* calculations for the ionization fraction (F) for different ions as a function of the product of gas density (n_{H}) (cm^{-3}) and time (yr). The ionization source is our AGN power-law ($f_{\nu} \propto \nu^{-1}$) model (Section 3); the addition of the “big blue bump” increases the timescale by a small factor. The radiation is hitting a cold slab of gas with subsolar metallicity ($Z = 0.1Z_{\odot}$). At the front face, the ionization parameter is $\log u = -3.0$ (top) and $\log u = -2.0$ (bottom).

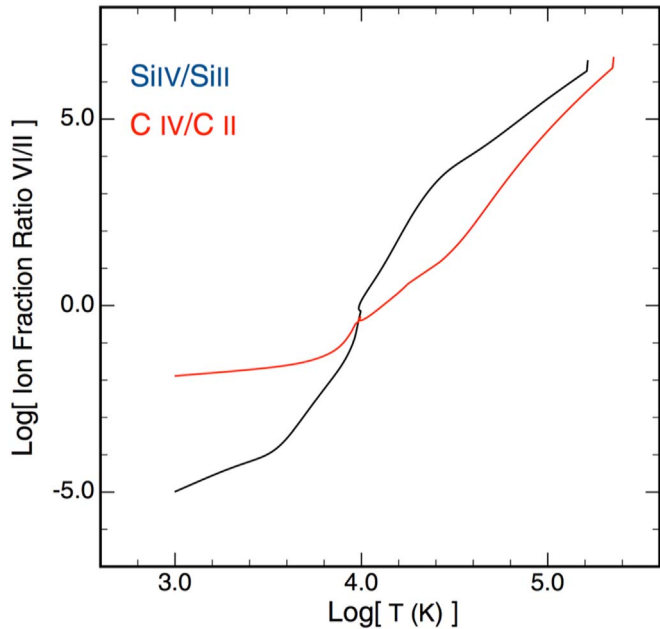


Figure 15. *Mappings V* calculations (assuming $Z = 0.1Z_{\odot}$) for the ratio of two ions in a cooling gas shown for C IV/C II and Si IV/Si II. The tracks cross at 10^4 K and above 10^5 K relevant to photoionization and moderate shock ($v_s \sim 100 \text{ km s}^{-1}$) zones, respectively.

these processes are possible at the Magellanic Stream’s distance over the SGP, where the coronal density is low ($\sim \text{few} \times 10^{-5} \text{ cm}^{-3}$).

Several authors have discussed the idea of conductive interfaces in which cool/warm clouds evaporate and hot gas condenses at a common surface where colliding electrons transport heat across a boundary (Gnat et al. 2010;

Armillotta et al. 2017). The gas tends to be “underionized” compared to gas in ionization equilibrium, which enhances cooling in the different ions. But Gnat et al. (2010) show that the nonequilibrium columns are always small ($\lesssim 10^{13} \text{ cm}^{-2}$) and an order of magnitude *below* the median columns detected by Fox et al. (2014).

For full consistency, the shock cascade model is an appropriate framework for a mixing layer calculation, but a self-consistent radiative MHD code to achieve this has yet to be developed. Our first models predict projected line broadening up to $\sigma \approx 20 \text{ km s}^{-1}$ in H I or warm ion transitions (Bland-Hawthorn et al. 2007). It is possible that, running models with intrinsically higher resolution, one can broaden the absorption-line kinematics and increase the column densities further through line-of-sight projections. An important future constraint is to map the relative distributions of warm ionized, warm neutral, and cold neutral hydrogen gas at high spectral/spatial resolution along the Magellanic Stream.

Currently, we do not find a compelling case for dominant processes beyond static photoionization from a distant source. All of these processes may have more relevance to the *Fermi* bubbles and to high-velocity clouds (HVCs) much lower in the Galactic halo ($D \ll 75 \text{ kpc}$). For the HVCs, such arguments have been made (Fox et al. 2005). Before an attempt is made to understand the Magellanic Stream in this context, it will be crucial to first demonstrate how turbulent mixing has contributed to UV diagnostics observed toward low-latitude clouds.

4.8. Correlations between the Observed Diagnostics along the Magellanic Stream

4.8.1. The Scatter in the $H\alpha$ Emission Relative to H I

Ideally, we would be able to bring together all spectroscopic information within a cohesive framework for the Magellanic Stream in terms of its origin, internal structure, ionization, and long-term evolution (e.g., Esquivel et al. 2006; Tepper-Garcia et al. 2015). As implied in the previous section, various parts of the problem have been tackled in isolation, but an overarching scheme covering all key elements does not exist today. For such a complex interaction, we must continue to gather rich data sets across the full electromagnetic spectrum (Fox et al. 2019). Our work has concentrated on both absorption and emission lines observed with very different techniques, effective beam sizes, and sensitivities. We now consider what one might learn in the future when both absorption and emission measures have comparable sensitivities and angular resolution. This may be possible in the era of extremely large telescopes (ELTs), at least for the $H\alpha$ -bright regions.

Figure 12 of Barger et al. (2017) shows the lack of any correlation between the $H\alpha$ detections and the projected H I column density. The emission measures mostly vary over about a factor of five, from ~ 30 to 160 mR ; there are two exceptionally bright knots along the Magellanic Stream with $400 \text{ mR} \lesssim \mu(\text{H}\alpha) \lesssim 600 \text{ mR}$. The total H column ($\text{H I} + \text{H}^+$) today is high enough to absorb a significant fraction of incident UV photons across much of the Magellanic Stream if the Sgr A* source currently radiates far below the Eddington limit. This simple observation is consistent with the nuclear flare having shut down and the Magellanic Stream’s recombination emission fading at a rate that depends only on the local gas density. For completeness, we mention one more possibility,

which is somewhat fine-tuned and therefore less plausible. It is possible that at the look-back time ($2T_c \approx 0.5$ Myr) at which we observe the Magellanic Stream emission (for a distance of 75 kpc) the Galaxy’s nuclear emission is still far above the present-day value and the spread in emission measures is dominated by column density variations along the lines of sight.

Assume for a moment that variations in N/N_{cr} are unimportant. In principle, the power spectrum of the $\text{H}\alpha$ patchiness constrains both the gas densities and the time since the radiation field switched off, since the scatter increases with the passage of time (up until the recombination time for the lowest-density gas is reached), due to the spread in τ_{rec} ; see Figure 4 in BH2013. However, there are several complications. The predicted range of $\mu_{\text{H}\alpha}$ as a function of time depends on the distribution of gas densities within the Magellanic Stream. At present, however, the observable range in $\text{H}\alpha$ surface brightness is limited by the moderate S/N of most of the detections.

An additional complication is that, at fixed density $\langle n_{\text{H}} \rangle$, lines of sight with $N < N_{\text{cr}}$ will be fainter in $\text{H}\alpha$ by the ratio N/N_{cr} , as discussed above. Finally, the observed patchiness is likely to be heavily filtered by the angular resolution of the observer’s beam (Tepper-Garcia et al. 2015). In the future, it may be possible to sort out these issues with knowledge of the *total* hydrogen column density along the Magellanic Stream from independent sources of information, e.g., soft X-ray shadowing by the Magellanic Stream projected against the cosmic X-ray background (e.g., Wang & Taisheng 1996).

4.8.2. The Scatter in the UV Absorption Lines Relative to H I

For absorption lines, it is the column density N_p that matters, not the product $n_e N_p$. In other words, the $\text{H}\alpha$ emission from low-density regions with large columns is, in effect, being scaled down by their low densities, but this is not true for the UV absorption lines. Hence, in this model, the prominence of the lowest-density regions in the absorption-line observations will be even more pronounced than it is for the $\text{H}\alpha$ emission: they not only stay more highly ionized for longer, because of the longer recombination times, but also arise in the largest H column densities (Figure 8), and that is what the absorption-line diagnostics are sensitive to.

What this argument does not determine is whether the carbon ionization state (as measured by the C IV/C II ratio) resembles what we are seeing for some reasonable period of time after the source turns off, or whether the only applicable models are ones in which the ionization state has not really had time to change. That still favors the lowest-density regions, however, for the reasons just outlined.

In general, for the assumed tubular geometry of the Magellanic Stream, we expect higher densities to roughly correspond to larger column densities. However, in the flare ionization model, as noted above, the densest regions recombine the fastest and thus fade quickly in $\text{H}\alpha$ and lose their C IV rapidly once the flare has switched off. In the flare model, as long as the gas column densities along the Magellanic Stream are greater than the critical column needed to soak up all of the ionizing photons, the density/column density anticorrelation (lower-density regions have larger ionized columns) is baked in by the physics, and so in this case we anticipate a positive correlation between the $\text{H}\alpha$ emission and the C IV absorption strength.

There are two caveats: the correlation (1) only arises if the low-density regions still have significant C IV fractions (i.e., they have not had time to recombine to low ionization states) and (2) would not hold if the C IV is coming mostly from regions where the density is so low that the total column is lower than the critical column, i.e., density-bounded rather than radiation-bounded sight lines. In the latter case, the $\text{H}\alpha$ emission will also be weaker than our model predicts, by the ratio of the actual column to the critical column. The H I/ $\text{H}\alpha$ comparison above was possible because of the comparable (0.1 – 1°) beam size for both sets of observations. Unfortunately, the UV absorption lines have an effective beam size that is orders of magnitude smaller than either the optical or radio detections. An additional problem are the short timescales associated with C IV recombination relative to $\text{H}\alpha$ and C II as we discuss below.

5. Discussion

There is nothing new about the realization of powerful episodic behavior erupting from the nuclei of disk galaxies (see Mundell et al. 2009). Some of these events could be close analogs to what we observe today in the Milky Way (see NGC 3079: Li et al. 2019; Sebastian et al. 2019). Since 2003, many papers present evidence for a powerful Galactic center explosion from radio, mid-infrared, UV, X-ray, and γ -ray emission. The remarkable discovery of the γ -ray bubbles (Su et al. 2010) emphasized the extraordinary power of the event. The dynamical (2–8 Myr) and radiative (2.5–4.5 Myr) timescales overlap, with possible evidence that the jet/wind break-out (Miller & Bregman 2016) preceded the radiative event (this work; BH2013). Conceivably, if the error estimates are reliable, this time difference is real, i.e. the explosive event was needed to clear a path for the ionizing radiation.

In the search for a singular event that may have triggered Sgr A* to undergo a Seyfert phase, we find the link to the central star streams and young clusters made by Zubovas & King (2012) to be compelling. Against a backdrop of ancient stars, Paumard et al. (2006) review the evidence for a young stellar ring with well-constrained ages of 4–6 Myr. The same connection may extend to the circumnuclear star clusters that fall within the same age range (Simpson 2018). Intriguingly, Kopusov et al. (2019) have recently discovered a star traveling at 1750 km s^{-1} that was ejected from the Galactic center some 4.8 Myr ago. It is tempting to suggest that this was also somehow connected with the major gas accretion event at that time, i.e., through stars close to the black hole being dislodged.

This could reasonably be made to fit with the shorter timescale ($T_o = 3.5 \pm 1$ Myr) for the flare if the event was sufficiently cataclysmic in the vicinity of Sgr A* to directly fuel the inner accretion disk. Accretion timescales of infalling gas being converted to radiative output can be as short as 0.1–1 Myr (Novak et al. 2011), although Hopkins et al. (2016) argue for a longer viscosity timescale. We now consider how the field can advance in future years with sufficient observational resources.

Toward a complete 3D map of halo clouds—The most successful approach for absorption-line detections along the Magellanic Stream has been to target UV-bright ($B < 14.5$) background AGNs and quasars (Fox et al. 2013, 2014). In the future, all-sky high-precision photometric imaging (e.g., LSST) will allow us to easily identify a population of UV-bright, metal-poor halo stars with well-established photometric

distances. Targeting some stars ahead and behind the Magellanic Stream will improve distance brackets for the Magellanic Stream and provide more information on the nature of the recent Seyfert outburst. There are many potential targets across the sky. The *Galaxia* model of the Galaxy (Sharma et al. 2011) indicates that there is one metal-poor giant per square degree brighter than $B = 14.5$ in the Galactic halo out to the distance of the Magellanic Stream, with a factor of six more at $B = 16$, which can be exploited in an era of ELTs. In principle, it will be possible to determine good distances to all neutral and ionized HVCs from distance bracketing across the entire halo, particularly within 50 kpc or so.

The high-velocity HI clouds lie almost exclusively close to the Galactic plane, i.e., outside the HI-free cones identified by Lockman & McClure-Griffiths (2016). There are highly ionized HVCs seen all over the sky found in O VI absorption but not in HI emission (Sembach et al. 2003). The O VI sky covering fraction is in the range of 60%–80%, compared to the HI covering fraction at about 40%. The use of near-field clouds to trace the ionization cones is hampered by the presence of ionized gas entrained by the X-ray/ γ ray bubbles (Fox et al. 2015; Bordoloi et al. 2017; Savage et al. 2017; Karim et al. 2018). But we anticipate that the ionization cones (Figure 2) and the *Fermi* bubbles (Figure 1) are filled with hundreds of distinct, fully ionized HVCs.

Magellanic Screen—viewing the AGN along many sight lines—The Magellanic Stream provides us with a fortuitous absorber for intersecting ionizing radiation escaping from the Galactic center. This “Magellanic Screen” extends over 11,000 deg² (Fox et al. 2014) and enables us to probe the complexity of the emitter over wide solid angles. Our simple adoption of the Madau model predicts a centrosymmetric pattern along some arbitrary axis. But many models produce anisotropic radiation fields, e.g., jets (Wilson & Tsvetanov 1994), thick accretion disks (Madau 1988), warped accretion disks (Phinney 1989; Pringle 1996), dusty tori (Krolik & Begelman 1986; Nenkova et al. 2008), and binary black holes. More measurements along the Magellanic Stream may ultimately shed more light on the recent outburst from Sgr A* and its immediate surroundings. The strongest constraint comes from variations in the ionization parameter u (Tarter et al. 1969), but detecting second-order effects from the spectral slope may be possible (e.g., Acosta-Pulido et al. 1990), although time-dependent ionization complicates matters (Section 4.4.2).

This suggests a future experiment. Consider an ionization pattern defined by an axis tilted with respect to the Galactic poles. Here we are assuming something like the C IV/C II line ratio to measure spectral “hardness” \mathcal{H} or ionization parameter u over the sky. We can now fit spherical harmonics to the all-sky distribution to establish the dominant axis of a centrosymmetric pattern (e.g., Fixsen et al. 1994). For illustration, we project our crude fit in Figure 9 as a sine wave in Magellanic longitude. To be useful, we need many more sight lines over the sky.

We are far from a convincing narrative for Sgr A*, as we are for any supermassive black hole. These fascinating sources are seeded and grow rapidly in the early universe and then accrete more slowly with the galaxy’s evolution over billions of years. Just how they interact and influence that evolution is an outstanding problem in astrophysics. We live in hope that this new work may encourage accretion disk modelers (e.g., GR-R-MHD codes; McKinney et al. 2014) to consider the UV

outburst in more detail and to predict the emergent radiation and timescale to aid future comparisons with observations. Ultimately, such models will need to be integrated into fully cosmological models of galaxy formation and evolution.

J.B.-H. is supported by a Laureate Fellowship from the Australian Research Council. J.B.-H. also acknowledges a 2018 Miller Professorship at UC Berkeley, where the first draft was completed. M.G. acknowledges funding from the University of Sydney. W.H.L. is supported by China-Australia Scholarship funds for short-term internships. We are particularly grateful to James Josephides (Swinburne University) and Ingrid McCarthy (ANU) for the movie rendition of the Magellanic Stream being ionized by the accretion disk around Sgr A* (see the caption to Figure 4). Over the past few years, we have benefitted from key insights and suggestions: we thank Chris McKee, Luis Ho, Jenny Greene, Will Lucas, Carole Mundell, Dipanjan Mukherjee, Roger Blandford, Lars Hernquist, Jerry Ostriker, Ramesh Narayan, and an anonymous referee, assuming, of course, that they are not in the list already.

Appendix A Emission Measures

In order to compare our model with the H α observations, we adopt physically motivated units that relate the ionizing photon flux at a distant cloud to the resultant H α emission. It is convenient to relate the plasma column emission rate to a photon surface brightness. Astronomical research on diffuse emission (e.g., WHAM survey—Reynolds et al. 1998) uses the Rayleigh unit introduced by atmospheric physicists (see Baker & Romick 1976), which is a unique measure of *photon* intensity; 1 millirayleigh (mR) is equivalent to $10^3/4\pi$ photons cm⁻² s⁻¹ sr⁻¹. The emission measure \mathcal{E}_m for a plasma with electron density n_e is given by (e.g., Spitzer 1978)

$$\mathcal{E}_m = \int f_i n_e^2 dz \quad \text{cm}^{-6} \text{ pc}, \quad (17)$$

which is an integral of H recombinations along the line of sight z multiplied by a filling factor f_i . The suffix i indicates that we are referring to the volume over which the gas is ionized. For a plasma at 10⁴ K, $\mathcal{E}_m(\text{H}\alpha) = 1 \text{ cm}^{-6} \text{ pc}$ is equivalent to an H α surface brightness of 330 mR. In cgs units, this is equivalent to $1.9 \times 10^{-18} \text{ erg cm}^{-2} \text{ s}^{-1} \text{ arcsec}^{-2}$, which is a faint spectral feature in a 1 hr integration using a slit spectrograph on an 8 m telescope. But for the Fabry–Perot “staring” technique employed in Figure 6, this is an easy detection if the diffuse emission uniformly fills the aperture. We refer to the Magellanic Stream H α emission as relatively bright because it is much brighter than expected for an optically thick cloud at a distance of 55 kpc or more from the Galactic center.

Appendix B Photoionization Due to a Seyfert Flare Event

Mappings V has been adapted to incorporate the time-dependent calculations in BH2013. Here a gas slab is ionized by a burst of radiation, which is then allowed to cool down over millions of years. These calculations, which use a wide range of ionizing sources (see Figure 10), are specifically aimed at C ions (Table 2) and Si ions (Table 3) observed at UV

wavelengths (e.g., Fox et al. 2014). A summary of the initial model parameters is given in Table 1.

ORCID iDs

Joss Bland-Hawthorn  <https://orcid.org/0000-0001-7516-4016>

Ralph Sutherland  <https://orcid.org/0000-0002-6620-7421>

Brent Groves  <https://orcid.org/0000-0002-9768-0246>

Andrew J. Fox  <https://orcid.org/0000-0003-0724-4115>

References

- Abramowicz, M. A., & Piran, T. 1980, *ApJL*, 241, L7
- Ackermann, M., Albert, A., Atwood, W. B., et al. 2014, *ApJ*, 793, 64
- Acosta-Pulido, J. A., Perez-Fournon, I., Calvani, M., & Wilson, A. S. 1990, *ApJ*, 365, 119
- Armillotta, L., Fraternali, F., Werk, J. K., Prochaska, J. X., & Marinacci, F. 2017, *MNRAS*, 470, 114
- Asplund, M. 2005, *ARA&A*, 43, 281
- Baker, D. J., & Romick, G. J. 1976, *ApOpt*, 15, 1666
- Balbus, S. A., & Hawley, J. F. 1991, *ApJ*, 376, 214
- Barger, K., Haffner, L. M., & Bland-Hawthorn, J. 2013, *ApJ*, 771, 132
- Barger, K. A., Madsen, G. J., Fox, A. J., et al. 2017, *ApJ*, 851, 110
- Begelman, M. C., & Bland-Hawthorn, J. 1997, *Natur*, 385, 22
- Begelman, M. C., & Fabian, A. C. 1990, *MNRAS*, 244P, 26B
- Besla, G., Kallivayalil, N., Hernquist, L. E., et al. 2007, *ApJ*, 668, 949
- Besla, G., Kallivayalil, N., Hernquist, L. E., et al. 2012, *MNRAS*, 421, 2109
- Bland-Hawthorn, J., & Cohen, M. 2003, *ApJ*, 582, 246
- Bland-Hawthorn, J., & Gerhard, O. 2016, *ARA&A*, 54, 529
- Bland-Hawthorn, J., & Maloney, P. R. 1999, *ApJL*, 522, L81
- Bland-Hawthorn, J., & Maloney, P. R. 2002, *ASPC*, 254, 267
- Bland-Hawthorn, J., Maloney, P. R., Sutherland, R. S., & Madsen, G. 2013, *ApJ*, 778, 58, (BH2013)
- Bland-Hawthorn, J., Sutherland, R. S., Agertz, O., & Moore, B. 2007, *ApJL*, 670, L109
- Bland-Hawthorn, J., Sutherland, R. S., & Webster, D. 2015, *ApJ*, 807, 154
- Bordoloi, R., Fox, A. J., Lockman, F. J., et al. 2017, *ApJ*, 834, 191
- Bower, G. C., & Backer, D. C. 1998, *ApJL*, 496, L97
- Bregman, J. N., Andersen, M. E., Miller, M. J., et al. 2018, *ApJ*, 862, 3
- Brüns, C., Kerp, J., Staveley-Smith, L., et al. 2005, *A&A*, 432, 45
- Carretti, E., Crocker, R. M., Staveley-Smith, L., et al. 2013, *Natur*, 493, 66
- Cooper, J., Bicknell, G. V., Sutherland, R. S., & Bland-Hawthorn, J. 2008, *ApJ*, 674, 157
- Di Teodoro, E. M., McClure-Griffiths, N. M., Lockman, F. J., et al. 2018, *ApJ*, 855, 33
- Done, S., Davis, S. W., Jin, C., Blaes, O., & Ward, M. J. 2012, *MNRAS*, 420, 1848
- d’Onghia, E., & Fox, A. J. 2016, *ARA&A*, 54, 363
- Dove, J., & Shull, M. M. 1994, *ApJ*, 430, 222
- Esquivel, A., Benjamin, R. A., Lazarian, A., et al. 2006, *ApJ*, 648, 1043
- Faerman, Y., Sternberg, A., & McKee, C. F. 2017, *ApJ*, 835, 52
- Fixsen, D. J., Cheng, E. S., Cottingham, D. A., et al. 1994, *ApJ*, 420, 445
- Fox, A. J., Barger, K. A., Bland-Hawthorn, J., et al. 2019, *BAAS*, 51, 20
- Fox, A. J., Bordoloi, R., Savage, B. D., et al. 2015, *ApJL*, 799, L7
- Fox, A. J., Lehner, N., Tumlinson, J., et al. 2013, *ApJ*, 772, 110
- Fox, A. J., Wakker, B. P., Barger, K. A., et al. 2014, *ApJ*, 787, 147
- Fox, A. J., Wakker, B. P., Savage, B. D., et al. 2005, *ApJ*, 630, 332
- Fox, A. J., Wakker, B. P., Smoker, J. V., et al. 2010, *ApJ*, 718, 1046
- Fujimoto, M., & Sofue, Y. 1976, *A&A*, 47, 263
- Fujimoto, M., & Sofue, Y. 1977, *A&A*, 61, 199
- Gnat, O., Sternberg, A., & McKee, C. F. 2010, *ApJ*, 718, 1315
- Gronke, M., & Oh, S. P. 2018, *MNRAS*, 480, L111
- Guglielmo, M., Lewis, G. F., & Bland-Hawthorn, J. 2014, *MNRAS*, 444, 1759
- Guo, F., & Mathews, W. G. 2012, *ApJ*, 756, 181
- Hillier, J. D. 2012, *IAU*, 282, 229
- Hopkins, A. M., & Beacom, J. F. 2006, *ApJ*, 651, 142
- Hopkins, P. F., & Hernquist, L. E. 2006, *ApJS*, 166, 1
- Hopkins, P. F., Torrey, P., Faucher-Giguère, C. A., Quataert, E., & Murray, N. 2016, *MNRAS*, 458, 816
- Inayoshi, K., Haiman, Z., & Ostriker, J. P. 2016, *MNRAS*, 459, 3738
- Ji, S., Oh, S. P., & Masterson, P. 2019, *MNRAS*, 487, 737
- Jin, C., Ward, M., Done, C., & Gelbord, J. 2012, *MNRAS*, 420, 1825
- Jin, S., & Lynden-Bell, D. 2008, *MNRAS*, 383, 1686
- Kaaret, P., Feng, H., & Roberts, T. P. 2017, *ARA&A*, 55, 303
- Kalberla, P. M., Burton, W. B., Hartmann, D., et al. 2005, *A&A*, 440, 775
- Kallivayalil, N., van der Marel, R. P., & Alcock, C. 2006, *ApJ*, 638, 772
- Kallivayalil, N., van der Marel, R. P., Besla, G., Anderson, J., & Alcock, C. 2013, *ApJ*, 764, 161
- Karim, M. T., Fox, A. J., Jenkins, E. B., et al. 2018, *ApJ*, 860, 98
- Koyama, K. 2018, *PASJ*, 70, 1
- Konz, C., Lesch, H., Birk, G. T., & Wiechen, H. 2001, *ApJ*, 548, 249
- Koposov, S., Boubert, D., Li, T. S., et al. 2019, *MNRAS*, submitted (arXiv:1907.11725)
- Kreimeyer, K., & Veilleux, S. 2013, *ApJL*, 772, L11
- Krolik, J. H., & Begelman, M. C. 1986, *ApJL*, 308, L55
- Kwak, K., & Shelton, R. L. 2010, *ApJ*, 719, 523
- Li, J.-T., Hodges-Kluck, E., Stein, Y., et al. 2019, *ApJ*, 873, 27
- Lockman, F. J., & McClure-Griffiths, N. 2016, *ApJ*, 826, 215
- Lucas, W. E., Bonnell, I. A., Davies, M. B., & Rice, W. K. M. 2013, *MNRAS*, 433, 353
- Madau, P. 1988, *ApJ*, 327, 116
- Madau, P., Haardt, F., & Dotti, M. 2014, *ApJ*, 784, 38
- Maloney, P. R. 1999, *Ap&SS*, 266, 207
- McKinney, J. C., Tchekhovskoy, A., Sadowski, A., & Narayan, R. 2014, *MNRAS*, 441, 3177
- McMillan, P. J. 2017, *MNRAS*, 465, 76
- Miller, M. J., & Bregman, J. N. 2016, *ApJ*, 829, 9
- Mukherjee, D., Wagner, A. Y., Bicknell, G. V., et al. 2018, *MNRAS*, 476, 80
- Mundell, C. G., Ferruit, P., Nagar, N., & Wilson, A. S. 2009, *ApJ*, 703, 802
- Nakashima, S., Nobukawa, M., Uchida, H., et al. 2013, *ApJ*, 773, 20
- Narayanan, S. A., & Slatyer, T. R. 2017, *MNRAS*, 468, 3051
- Nataf, D. 2016, *PASA*, 33, 23
- Neškova, M., Strocky, M., Nikutta, R., et al. 2008, *ApJ*, 685, 160
- Nichols, M., Colless, J., Colless, M. M., & Bland-Hawthorn, J. 2011, *ApJ*, 742, 110
- Nidever, D. L., Majewski, S. R., & Butler, W. B. 2008, *ApJ*, 679, 432
- Nidever, D. L., Majewski, S. R., Butler, W. B., & Nigröu, L. 2010, *ApJ*, 723, 1618
- Nigra, L., Stanimirović, S., Gallagher, J. S., et al. 2012, *ApJ*, 760, 48
- Novak, G., Ostriker, J., & Ciotti, L. 2011, *ApJ*, 737, 26
- Novikov, I. D., & Thorne, K. S. 1973, in *Astrophysics of Black Holes*, ed. C. DeWitt & B. DeWitt (New York: Gordon and Breach), 343
- Paczynski, B., & Wiita, P. J. 1980, *A&A*, 88, 23
- Paumard, T., Genzel, R., Martins, F., et al. 2006, *ApJ*, 643, 1011
- Phinney, E. S. 1989, *IAU*, 146, 543
- Pogge, R. 1988, *ApJ*, 328, 519
- Pringle, J. E. 1996, *MNRAS*, 281, 357
- Putman, M. E., Bland-Hawthorn, J., Veilleux, S., et al. 2003, *ApJ*, 597, 948
- Putman, M. E., Gibson, B. K., Staveley-Smith, L., et al. 1998, *Natur*, 394, 752
- Rees, M. J., & Volonteri, M. 2007, in *IAU Symp. 238, Black Holes from Stars to Galaxies—Across the Range of Masses*, ed. V. Karas & G. Matt (Cambridge: Cambridge Univ. Press), 51
- Reynolds, R. J., Tufté, S., Haffner, L. M., et al. 1998, *PASA*, 15, 14
- Richter, P., Fox, A. J., Wakker, B. P., et al. 2013, *ApJ*, 772, 111
- Savage, B. D., Kim, T. S., Fox, A. J., et al. 2017, *ApJS*, 232, 25
- Sebastian, B., Kharb, P., O’Dea, C. P., et al. 2019, *ApJ*, 883, 189
- Sembach, K., Wakker, B. P., Savage, B. D., et al. 2003, *ApJS*, 146, 165
- Sharma, S., Bland-Hawthorn, J., Johnstone, K., & Binney, J. 2011, *ApJ*, 730, 3
- Sharp, R. G., & Bland-Hawthorn, J. 2010, *ApJ*, 711, 818
- Simpson, J. P. 2018, *ApJ*, 857, 59
- Soltan, A. 1982, *MNRAS*, 200, 115
- Spitzer, L. 1978, *Physical Processes in the Interstellar Medium* (New York: Wiley)
- Stanimirović, S., Hoffman, S., Heiles, C., et al. 2008, *ApJ*, 680, 276
- Su, M., & Finkbeiner, D. P. 2012, *ApJ*, 753, 61
- Su, M., Slatyer, T. R., & Finkbeiner, D. P. 2010, *ApJ*, 724, 1044
- Sutherland, R. S. 2010, *Ap&SS*, 327, 173
- Sutherland, R. S., & Dopita, M. A. 2017, *ApJS*, 229, 34
- Tarter, C. B., Tucker, W. H., & Salpeter, E. E. 1969, *ApJ*, 156, 943
- Tepper-García, T., Bland-Hawthorn, J., Pawłowski, M. S., & Fritz, T. K. 2019, *MNRAS*, 488, 918
- Tepper-García, T., Bland-Hawthorn, J., & Sutherland, R. S. 2015, *ApJ*, 813, 94
- The GRAVITY Collaboration, Abuter, R., Amorim, A., et al. 2019, *A&A*, in press (arXiv:1904.05721)
- Tsvetanov, Z., Morse, J. A., Wilson, A. S., & Cecil, G. N. 1996, *ApJ*, 458, 172
- Vieser, W., & Hensler, G. 2007, *A&A*, 475, 251
- Volonteri, M. 2010, *A&A Reviews*, 18, 279

- Wang, Q. D., & Taisheng, Y. 1996, [NewA](#), **1**, 245
- Weiner, B. J., Vogel, S. N., & Williams, T. B. 2002, in ASP Conf. Ser. 254, Extragalactic Gas at Low Redshift, ed. J. S. Mulchaey & J. Stocke (San Francisco, CA: ASP), 26
- Weiner, B. J., & Williams, T. B. 1996, [AJ](#), **111**, 1156
- Weymann, R. J., Vogel, S. N., Veilleux, S., & Epps, H. W. 2001, [ApJ](#), **561**, 559
- Wilson, A. S., & Tsvetanov, Z. I. 1994, [AJ](#), **107**, 1227
- Yang, H. Y., Ruszkowski, M., & Zweibel, E. 2018, [Galax](#), **6**, 29
- Yelda, S., Ghez, A. M., Lu, J. R., et al. 2014, [ApJ](#), **783**, 131
- Yu, Q., & Tremaine, S. D. 2002, [MNRAS](#), **335**, 965
- Zhang, X., & Lu, Y 2019, [ApJ](#), **873**, 101
- Zovaro, H. R. M., Sharp, R. G., Nesvadba, N. P. H., et al. 2019, [MNRAS](#), **484**, 3393
- Zubovas, K., & King, A. R. 2012, [ApJ](#), **745**, 34
- Zubovas, K., & Nayakshin, S. 2012, [MNRAS](#), **424**, 666